ScieRxiv
NOT PEER-REVIEWED
Original Article

Three-dimensional culture reshapes extracellular vesicle profiles as revealed by super-resolution nanoimaging, next-generation sequencing, and proteomic analyses

Megan I. Mitchell[1], Vamsikrishna R. Vaidyula[1,2], Chunyan Hou[3], Iddo Z. Ben-Dov[4], Erik DeJonge[1,5], Christina Liu[1], Elizabeth Pinsky[6], Alexander Spark[7], Alexandre Kitching[7], Junfeng Ma[3] and Olivier Loudig[1]

[1]Center for Discovery and Innovation, Hackensack Meridian Health (HMH), Nutley, NJ 07110-5100, USA.
[2]Department of Biology, Drew University, Madison, NJ 07940, USA.
[3]Department of Oncology, Lombardi Comprehensive Cancer Center, Georgetown University Medical Center, Washington DC, 20007, USA.
[4]Department of Nephrology and Hypertension, Hadassah - Hebrew University Medical Center, Jerusalem 91120, Israel.
[5]School of Graduate Studies, University of Skövde, Högskolevägen 541 45, Sweden.
[6]Bergen County Technical High School, Teterboro, NJ07608, USA.
[7]Nanometrix, London SE1 2BE, UK.

Correspondence to: Dr. Olivier Loudig, Center for Discovery and Innovation, Hackensack Meridian Health (HMH), Nutley, NJ 07940, USA. Email: olivier.loudig@hmh-cdi.org

Received: 21 October 2026 | Approved: 26 October 2026 | Online: 26 October 2026

Abstract

Extracellular vesicles (EVs) are critical mediators of intercellular communication and promising cancer biomarkers; however, identifying EVs derived from specific tissues or cell

© The Author(s) 2026. Open Access This article is licensed under a Creative Commons Attribution 4.0 International License (https://creativecommons.org/licenses/by/4.0/), which permits unrestricted use, sharing, adaptation, distribution and reproduction in any medium or format, for any purpose, even commercially, as long as you give appropriate credit to the original author(s) and the source, provide a link to the Creative Commons license, and indicate if changes were made.

populations within complex biofluids, and selectively isolating them, remains a major challenge. The *in vitro* culture of defined human cell populations offers an accessible source of cell-specific EVs for their molecular characterization; however, conventional two-dimensional (2D) culture fails to recapitulate key features of three-dimensional (3D) *in situ* tumor architecture. Here, we conducted a controlled comparative analysis of small EVs derived from the immortalized human cervical cancer cell line Ca Ski cultured as 2D monolayers and 3D Matrigel-embedded spheroids to investigate how cellular architecture influences small EV production and molecular composition. Small EVs were isolated from conditioned media by ultracentrifugation and characterized by Spectradyne nanoparticle analysis, transmission electron microscopy (TEM), and ONi super-resolution imaging coupled with AI-guided Nanometrix topological analyses. Small EVs were efficiently recovered from the conditioned media of both culture conditions, although 3D cultures yielded approximately ten-fold fewer nanoparticles while exhibiting an increased relative abundance of vesicles within the 80-110 nm size range compared with 2D cultures. Topological analyses of small-EV-associated tetraspanins (CD63, CD81, CD9) revealed distinct profiles between culture conditions, with increased proportions of CD81-positive and CD63/CD81 double-positive vesicles in 3D-derived isolates, while CD63 single-positive vesicles were enriched in 2D-derived isolates. Complementary RNA sequencing and proteomic analyses revealed that 2D- and 3D-derived small EVs were packaged with distinct molecular cargo, while supporting consistent detection of miRNAs, tRNA-derived fragments, and approximately 2,000 proteins across both culture conditions. Notably, miRNAs enriched in 2D-derived small EVs were predicted to regulate translation of proteins and pathways enriched in 3D-derived small EVs, suggesting coordinated remodeling of EV cargo in response to cellular architecture. Collectively, these findings demonstrate that culture conditions influence both the physical characteristics and molecular composition of small EV populations and support the use of 3D culture as a relevant model for investigating small EV biology.

Keywords: Extracellular vesicles, exosomes, small-RNA, microRNA, transfer RNA fragments, next-generation sequencing, cDNA library, transmission electron microscopy,

nanoparticle analyzer, PCR, tissue culture, Matrigel, ultracentrifugation, data-independent acquisition (DIA) mass spectrometry

INTRODUCTION

Cervical cancer remains a significant public health challenge despite advances in screening and prevention[1,2]. In the United States, an estimated 13,800 new cases of invasive cervical cancer and more than 4,300 deaths occur annually, making it a leading cause of cancer-related mortality among women of reproductive age. Although widespread implementation of Papanicolaou (Pap) cytology and human papillomavirus (HPV) screening, together with the introduction of HPV vaccination, has contributed to substantial reductions in cervical cancer incidence and mortality, these benefits have not been equally realized across all populations. Disparities in screening access, follow-up care, and disease outcomes persist, with medically underserved populations and racial and ethnic minorities continuing to experience a disproportionate burden of cervical cancer[3,4].

Persistent infection with high-risk human papillomavirus (HPV) types is the principal driver of cervical carcinogenesis; however, only a subset of individuals with persistent infection ultimately develop high-grade cervical lesions or invasive disease[5,6]. This biological heterogeneity highlights a critical limitation of current screening paradigms, which remain limited in their ability to distinguish transient HPV infections from lesions with a greater likelihood of malignant progression. Consequently, some patients undergo repeated surveillance and invasive diagnostic procedures, while others experience delayed diagnosis and poorer outcomes[7].

Once cervical cancer progresses beyond early-stage disease, prognosis worsens substantially, and therapeutic options become increasingly limited. Five-year survival rates decline sharply with advancing disease stage, underscoring the need for biomarkers that can facilitate earlier detection, improve risk stratification, and enable real-time monitoring of disease progression and treatment response[1,8]. The development of circulating molecular biomarkers capable of non-invasively capturing tumor-derived biological signals could therefore significantly improve cervical cancer detection and management.

Among emerging biomarker approaches, tissue-specific small extracellular vesicles (small EVs) have gained increasing attention as a promising source of circulating molecular biomarkers. Small EVs are membrane-bound nanoscale particles released by virtually all cell types and present in most biofluids[9,10]. These nanoparticles carry diverse molecular cargo, including proteins, lipids, and nucleic acids, that reflect the active cellular processes of their cells of origin[11-13]. Through the transfer of biologically active cargo between cells, small EVs mediate intercellular communication and have been implicated in numerous biological processes, including tissue homeostasis, immune modulation, and disease progression[14-18].

Of the diverse molecular cargo carried by small EVs, microRNAs (miRNAs) have received particular attention because of their ability to coordinately regulate gene expression in recipient cells, their remarkable stability within EVs, and the association of their expression profiles with the biological state of their cells of origin[19]. Notably, the miRNA composition of tumor-derived small EVs can differ substantially, both qualitatively and quantitatively, from that of small EVs released by non-malignant cells and tissues[20-22]. Consequently, cell- and tissue-specific EV-associated miRNAs are increasingly being explored as minimally invasive biomarkers for cancer detection, prognosis, and therapeutic monitoring[23-25]. In addition to RNA cargo, small EV-associated proteins provide complementary information regarding the cellular state and biological processes of their cells of origin, and proteomic profiling of small EVs has emerged as an important strategy for identifying disease-associated molecular signatures and candidate biomarkers[26,27]. Importantly, incorporation of both miRNAs and proteins into small EVs is increasingly recognized as a regulated biological process rather than a purely passive event. miRNA sorting can be influenced by RNA sequence motifs, RNA-binding proteins, and intracellular signaling pathways, while selective protein incorporation is likewise influenced by cellular trafficking and sorting machinery, post-translational modifications, and interactions with vesicular membrane and cytosolic components[28-33].

Recent studies suggest that small EV biogenesis, secretion, and molecular cargo composition may also be influenced by the cellular microenvironment[34]. Despite this, most *in vitro*

studies of small EV biology continue to rely on conventional two-dimensional (2D) monolayer culture systems[35]. Although 2D cultures provide a reproducible and accessible system for EV production, isolation, and characterization, they fail to recapitulate key aspects of the *in vivo* tumor microenvironment, including three-dimensional tissue architecture, extracellular matrix interactions, oxygen and nutrient gradients, cell-to-cell interactions, and mechanical forces[36-38]. These differences may alter cellular behavior and consequently influence the abundance, physical characteristics, and molecular composition of EV populations generated under 2D culture conditions. In contrast, three-dimensional (3D) culture systems have gained increasing attention because they more closely reproduce native tissue organization and key features of the tumor microenvironment that influence cellular metabolism, differentiation, signaling, and gene expression[39-41]. Emerging evidence suggests that these environmental differences may also affect small EV biogenesis, secretion, and molecular cargo composition, including EV-associated miRNAs and proteins[42-47]. Nevertheless, systematic studies directly examining how culture dimensionality influences small EV abundance, physical properties, surface-marker topology, and associated small RNA and protein cargo under otherwise matched experimental conditions remain limited.

Understanding the influence of culture dimensionality on small EV composition is particularly important for translational applications. Small EVs generated from *in vitro* cancer models are widely used to investigate tumor biology, identify candidate biomarkers, and evaluate therapeutic responses[48]. If EV-associated miRNA and protein profiles are influenced by culture dimensionality, then the cellular environment in which tumor cells are maintained represents an important experimental variable when interpreting small EV molecular profiles[49,50]. Experimental systems that more closely recapitulate *in vivo* tumor architecture may therefore improve the biological interpretation of EV-derived molecular signatures and their use for candidate biomarker discovery. This consideration is particularly relevant to cervical cancer, where the cellular origins of circulating small EV populations remain incompletely defined, highlighting the need for controlled model systems that enable the production and molecular characterization of cervical tumor cell-derived small EVs prior to their isolation and investigation in patient biofluids.

In this study, following the Minimal Information for Studies of Extracellular Vesicles (MISEV) guidelines[51], we performed a controlled comparison of small EVs produced by the well-characterized human Ca Ski cervical cancer cell line cultured under matched two-dimensional (2D) monolayer and three-dimensional (3D) Matrigel-embedded spheroid conditions. To minimize biological and technical variability, identical cell numbers were seeded using the same six-well culture format, with the principal experimental difference being the introduction of a three-dimensional extracellular matrix environment using Matrigel. This controlled design enabled us to investigate the influence of culture dimensionality and three-dimensional cellular architecture on small EV production, physical characteristics, and molecular composition. Using complementary analytical approaches, including nanoparticle analysis, transmission electron microscopy, super-resolution nanoimaging of EV-associated surface tetraspanins, small RNA next-generation sequencing (NGS), and mass spectrometry-based proteomics, we characterized small EV populations generated under both culture conditions. This integrated approach allowed us to determine whether differences in cellular architecture were associated not only with changes in small EV abundance and physical characteristics but also with differences in their small RNA and protein cargo. Importantly, this experimental system also enabled us to establish the feasibility of isolating small EVs from Matrigel-embedded cervical cancer cultures and to define experimental parameters for their reproducible production, isolation, and molecular profiling. Together, these studies provide a foundation for the future investigation of cervical tumor-derived small EVs and their associated molecular biomarkers using patient-derived organoid models.

MATERIALS AND METHODS

Ca ski cell culture

Ca Ski cervical cancer cells (ATCC; cat#CRL-1550) were used for *in vitro* 2-Dimensional (i.e., 2D in monolayer in 6 well-plates) and 3-Dimensional (i.e., 3D in Matrigel Matrix for Organoid Culture (Corning, cat#356255) in 6 well-plates) tissue culture experiments. Cells were maintained in RPMI-1640 medium (Gibco™, Cat#11875093) supplemented with 10% exosome depleted fetal bovine serum (FBS, Gibco™, Cat#A2720801) and 1% penicillin-streptomycin (Gibco™, Cat#15140148). For both 2D and 3D cell culture, Ca Ski cells

(ATCC®) were seeded at a density of 1 × 10^6 cells per well in 6-well plates, either directly on the bottom of the wells (2D) or within Matrigel (3D; 500 µL cell suspension containing 3 × 10^6 cells with 500 µL Matrigel to produce 21 Matrigel domes each of 45 µL, with 7 domes plated per well). Each 6-well plate was divided into three experimental wells (top row) and three control wells (bottom row) for 2D and 3D culture. All wells of the 6 well-plates contained 2 mL media. The control wells contained either 2 mL of cell-free media (2D minus) or 2 mL of media added onto cell-free Matrigel domes (3D minus). All 6-well plates were incubated at 37 °C with 5% CO_2 for 96 h. Conditioned media was collected after 48 h, followed by replenishment with fresh overlay media, and with a second harvest at 96 h. A total of 10-12 mL media was collected and combined from the experimental wells (*i.e.,* 3x ~2 mL at 48 h and 3x ~2 mL at 96 h) and 10-12 mL media was collected from the control wells (*i.e.,* 3x ~2 mL at 48 h and 3x ~2 mL at 96 h). Media collected at 48 h was stored at 4°C and then combined with media collected at 96 h to undergo ultracentrifugation. These experiments were conducted 6 times to produce replicates, with sufficient available biological material, to conduct our analyses. For 2D cultured cells, 1 mL TrypLE™ Express Enzyme (Gibco™, Cat#12604013) per well was applied per well and incubated for 10 min at 37 °C to detach cells, which were washed in 15 mL phosphate-buffered saline (1x PBS; Gibco™, Cat#10010023), prior to being pelleted, re-suspended in media and re-pelleted.

Ultracentrifugation

Tissue culture media temporarily stored at 4 °C (1 to 4 days) was Ultracentrifuged (UC) using a SW41 Ti rotor (Beckman Coulter) with Ultraclear 13.2 mL open-top Thinwall Ultra-Clear UC tubes (Beckman Coulter. Cat#344059) following a previously described procedure[52,53]. In brief, an average of 10 mL of each type of conditioned media was added to Ultraclear UC tubes and subjected to 10,000 × *g* centrifugation for 30 min. The supernatant was then transferred into fresh Ultraclear UC tubes and underwent an overnight ultracentrifugation (~16-20 h) step at 100,000 × *g*. The supernatants were carefully removed and discarded, while pelleted EV were resuspended with 5 mL of 1x PBS (Gibco™, Cat#10010023), to undergo a final spin of 100,000 × *g* for 2 h. The supernatants were discarded, and the small EV pellets were resuspended in 50 mL 1x PBS and transferred into low bind Eppendorf tubes for storage at -80 °C until further processing.

RNA extraction

EV isolated from the media of 2D and 3D culture condition by ultracentrifugation underwent RNA extraction using the *miRNeasy Serum/Plasma Kit* (Qiagen, Cat#217184) following the manufacturer's protocol. All samples were treated with RNAse A (Thermo Scientific, Cat#EN0531) for 15 min prior to RNA extraction. Water controls, media from 2D culture 6 well-plates without cells; and media incubated with matrigel domes without cells for 96 h, all also underwent RNA extraction using the *miRNeasy Serum/Plasma Kit* (Qiagen). RNA bound to the minelute columns of the *miRNeasy Serum/Plasma Kit* (Qiagen) was eluted using 18 µL of RNase-free water. QPCR analyses of microRNA-21 were conducted on un-diluted RNA extracts, prior to small-RNA cDNA library preparation. The quality of EV RNA and RNA from media without cells was also evaluated on the Agilent Tapestation.

Extracellular vesicle (EVs) analyses

EVs isolated by ultracentrifugation were initially quantified using C-400 cartridges (~65-400 nm particle count) on a Spectradyne nCS1 instrument and software. One microliter of EV solution was diluted with 399 µL of 1x PBS, 1%Tween solution and quantified based on size. Subsequently, ONi Super Resolution Nanoimaging was conducted using the human EV profiler 2 kit (ONi, San Diego, USA), with fluorescently labeled anti-CD9 (Alexa Fluor (AF) 488), anti-CD81 (AF-647), and anti-CD63 (AF-568) antibodies. Images generated by the ONi instrument were initially analyzed using the CODI software provided by ONi, following manufacturer's instructions. To enhance the depth of the EV imaging analyses, the Nanometrix software (Nanometrix, Inc., London, UK) was then utilized by averaging the values of 6 regions of interest (ROI) per lane (i.e., per sample). Biological repeats were analyzed together, by combining their ROIs (i.e., 12 ROIs per group). The data extracted by this software enabled EV size evaluation and the distribution of the CD9, CD81, and CD63 tetraspanins based on particle size, between different samples and conditions.

Quantitative PCR analyses

Initial qPCR analyses were conducted against miR-21, as an estimated measure of overall RNA concentration to normalize RNA input prior to cDNA library preparation. The

Taqman® miRNA reverse transcription kit, Taqman® universal PCR master mix, No AmpErase® UNG (Applied Biosystems, Cat#4364343), and the Taqman® miR-21 primer kit were utilized to conduct the RT and then PCR reactions, following manufacturer's instructions. PCR quantifications were conducted on a QuantStudio 6.0 instrument. Comparative thresholds (Ct) were determined by averaging the results of triplicate PCR reactions. The ΔCt of each miR-21 was determined by subtracting the mean Ct value of samples containing RNA (i.e., EVs) from the Ct of RNA isolated from 2D media alone (incubated without cells), and from 3D media alone (incubated without cells) for 2D and 3D RNA evaluation analyses. The fold-change differences were calculated using the 2e(ΔΔCt) formula.

Small-RNA cDNA library preparation and next generation sequencing (NGS)

For these analyses we utilized the cDNA library preparation protocol recently described in Loudig *et al.* 2024[54], which enables the preparation of amplicons compatible with the Illumina NextSeq2000 instrument. In brief, total cellular RNA, quantified by qPCR analysis of miR-21 in comparison to miR-21 abundance in EVs, was diluted prior to preparation of cDNA libraries. An average of 1.35-2.4ng of total RNA was utilized for the library preparation of cellular RNA (i.e., 2D and 3D cells). A total of 16 RNA samples was ligated to 16 individual barcoded 3' adenylated adapters using T4 RNA ligase 2, truncated (K227Q) (NEB; Cat#M0351S) at 4 °C for 16h. The next day, the 16 reactions were heat-inactivated, and the ligated products combined, precipitated in presence of NaCl, and size-selected on a 15% polyacrylamide gel (PAGE). The ligated products were excised, purified, and subjected to a 5 'adapter ligation in presence of T4 RNA ligase 1 (NEB; Cat#M0204S) at 37 °C for 1h. After this second ligation, the products were size-selected on a 15% polyacrylamide gel (PAGE), purified, precipitated, resuspended, reverse-transcribed, and the cDNA templates were subjected to 24 PCR cycles. The PCR products were size selected on a 2% agarose gel, purified, and then used in a second PCR reaction for 9 cycles, in presence of Illumina adapters compatible with the Illumina NextSeq 2000 sequencer. Two libraries were analyzed during a single run on a NextSeq 1000/2000 P2 100-cycle cartridge, which produces a total of 490 million reads, of which 230 million were attributed to this library. Calibrator oligonucleotides, included in the initial ligation, were used as quality control to evaluate the enzymatic and

experimental steps followed during cDNA library preparation. NGS reads were demultiplexed with the 16 barcodes and aligned to the HG6 human genome using both the RNAworld pipeline developed and owned by the laboratory of Dr. Thomas Tuschl and the miRge3.0 pipeline[55].

Quantitative proteomics analysis of EVs

EV samples from 2-D 3-D cultured CaSki cells were subjected to quantitative proteomics analysis, by following procedures in our previous work[56,57]. In brief, proteins were extracted from EVs by using 5% SDS in 50 mM triethylammonium bicarbonate (TEABC), followed by reduction with 20 mM DTT and alkylation with 45 mM of iodoacetamide. Proteins were then digested on a S-Trap column (ProtiFi, LLC) with sequencing-grade trypsin/Lys-C (Promega). The resulting peptides were analyzed with a nanoElute 2 system (Bruker) coupling with a timsTOF Ultra II mass spectrometer (Bruker) in dia-PASEF mode, with parameters similar to those described previously[58]. The DIA data files were processed by Spectronaut (Biognosys, v20) using standard settings with slight modifications. In brief, dynamic retention time prediction with local regression calibration was selected. Interference correction on MS and MS2 levels was enabled. The Q value cutoff was set to 1% at peptide precursor and protein levels using scrambled decoy generation and dynamic size at 0.1 fraction of library size. MS2-based quantification by area was used, enabling local cross-run normalization. We also performed biostatistics for the sample pairs. Proteins showing fold changes either > 1.5 (increase) or < 0.66 (decrease) and Q values (adjusted *p* values) < 0.05 were considered as significantly changed ones between groups.

Small-RNA sequencing and differential expression analysis

Raw small-RNA sequencing reads, aligned using both the RNAworld pipeline[59] and miRge3.0[55], were compiled into count matrices for microRNAs (miRNAs) and transfer RNA-derived fragments (tRFs) across all experimental conditions. Low-abundance features were removed prior to differential expression analysis using the filterByExpr function from edgeR (version 4.8.0)[60], which applies an adaptive threshold based on library size and experimental design. Count matrices were then used to construct objects for downstream analysis. Differential expression testing was performed using DESeq2 (version 1.50.2)[61]. *P*-

values were adjusted for multiple testing using the Benjamini-Hochberg procedure, and features with an adjusted *p*-value < 0.05 were considered statistically significant. For principal component analysis (PCA) and heat map visualization, count data were transformed using the variance-stabilizing transformation (VST) implemented in DESeq2. Two complementary approaches were used for heat map generation. For the global overview heat maps, TMM-normalized (trimmed mean of M-values) counts were computed using edgeR, $\log_2$-transformed relative to library size, and visualized using the heatmap function from the NMF R package[62] with Canberra distance and default hierarchical clustering [Supplementary Figure 2, Supplementary Figure 3b, Supplementary Figure 4, Figure 4d]. For the focused 2D versus 3D small EV comparison heatmaps [Figure 4d], VST-transformed counts for the top 25 differentially expressed features (ranked by adjusted p-value) were row-scaled (z-score) and clustered using Euclidean distance with the Ward.D2 agglomeration method. Volcano plots were generated using ggplot2 to visualize the relationship between $\log_2$ fold change and statistical significance ($-\log_{10}$ adjusted *p*-value) for both miRNAs and tRFs in the 2D versus 3D small EV comparison. All bioinformatic and statistical analyses were performed in R (version 4.5.2; R Foundation for Statistical Computing, Vienna, Austria). Code files are available from the authors upon request.

Pathway enrichment and miRNA-protein analysis

To evaluate the functional pathways associated with the significantly altered proteins, UniProt accession numbers were separately extracted for proteins upregulated in the 2D and 3D EV models. Each protein list was submitted to the Database for Annotation, Visualization, and Integrated Discovery (DAVID; v2025)[63] for Gene Ontology (GO) annotation across three ontologies: molecular function, biological process, and cellular component. The resulting GO terms and their associated *p*-values, adjusted for multiple testing using the Benjamini-Hochberg method, were submitted to Reduce and Visualize Gene Ontology (REVIGO; v1.8.1) to summarize redundant annotations and visualize inter-term relationships[64]. REVIGO clustered semantically similar GO terms to identify predominant biological processes represented by the proteins. Key GO associations were further investigated using the KEGG Pathways tool in DAVID, which maps proteins to established biological pathways. This analysis contextualized the condensed GO term data and identified

metabolic and signaling pathways associated with the proteins. Relevant KEGG pathways, gene counts, raw *p*-values, and Benjamini-adjusted *p*-values were collected and used to generate pathway enrichment plots in R (v4.6.1).

Potential regulatory relationships between miRNAs enriched in 2D EVs and proteins enriched in 3D EVs were then evaluated. 2D-enriched miRNAs were identified based on average $\log_2$ fold ratios, base counts, and p-values. Selection thresholds were set at a raw *p*-value ≤ 0.011 and base counts ≥ 135 to expand the candidate miRNA pool while limiting less-stringent candidates. Selected miRNAs were submitted to miRWalk (v3.0)[65,66] to predict target genes, which were compared with 3D-enriched EV protein-coding genes using Venny (v2.1.0) to identify overlaps. The overlapping gene set was then analyzed using the KEGG Pathways tool in DAVID to determine whether predicted miRNA targets were enriched in pathways represented by 3D-enriched proteins. Relevant KEGG pathways, gene counts, raw *p*-values, and Benjamini-adjusted *p*-values were collected and used to generate a comparative pathway enrichment plot in R.

RESULTS

Experimental design

In this study, we used the human Ca Ski epithelial-like cervical cancer cell line to perform comparative analyses of small EVs isolated from conditioned media generated under traditional two-dimensional (2D) monolayer culture and three-dimensional (3D) spheroid culture conditions as outlined in Figure 1. Cells were cultured in six well-plates for both 2D and 3D conditions. For each culture condition, three of the six wells contained media alone without cells (no cell control; Ctl) and three wells containing Ca Ski cells (see representative bright-field images in Figure 1). Conditioned media from these four experimental groups (2D Ctl, 2D Ca Ski, 3D Ctl, and 3D Ca Ski) was collected at both 48 h and 96 h post seeding (Figure 1; Green square for media without cells in 2D (#1), Pink square for media from Ca Ski cells in 2D (#2), Dark blue square for media without cells in 3D (#3), and Light blue square for media from Ca Ski cells in 3D conditions(#4)). At both timepoints (48h and 96h), 2 mL of media was collected from each of the three wells per condition. Collected media was centrifuged to remove cells and debris, followed by ultracentrifugation to isolate small EVs

using our previously described procedure[52,53]. This experimental design generated four independent sample types, namely, 1) 2D media alone (2D no cell Control), 2) 2D Ca Ski cell media, 3) 3D media alone (3D no cell control) and 4) 3D Ca Ski cell media. This side-by-side 2D and 3D culture model was repeated six independent times, generating technical replicates 1 through 6, for downstream analyses.

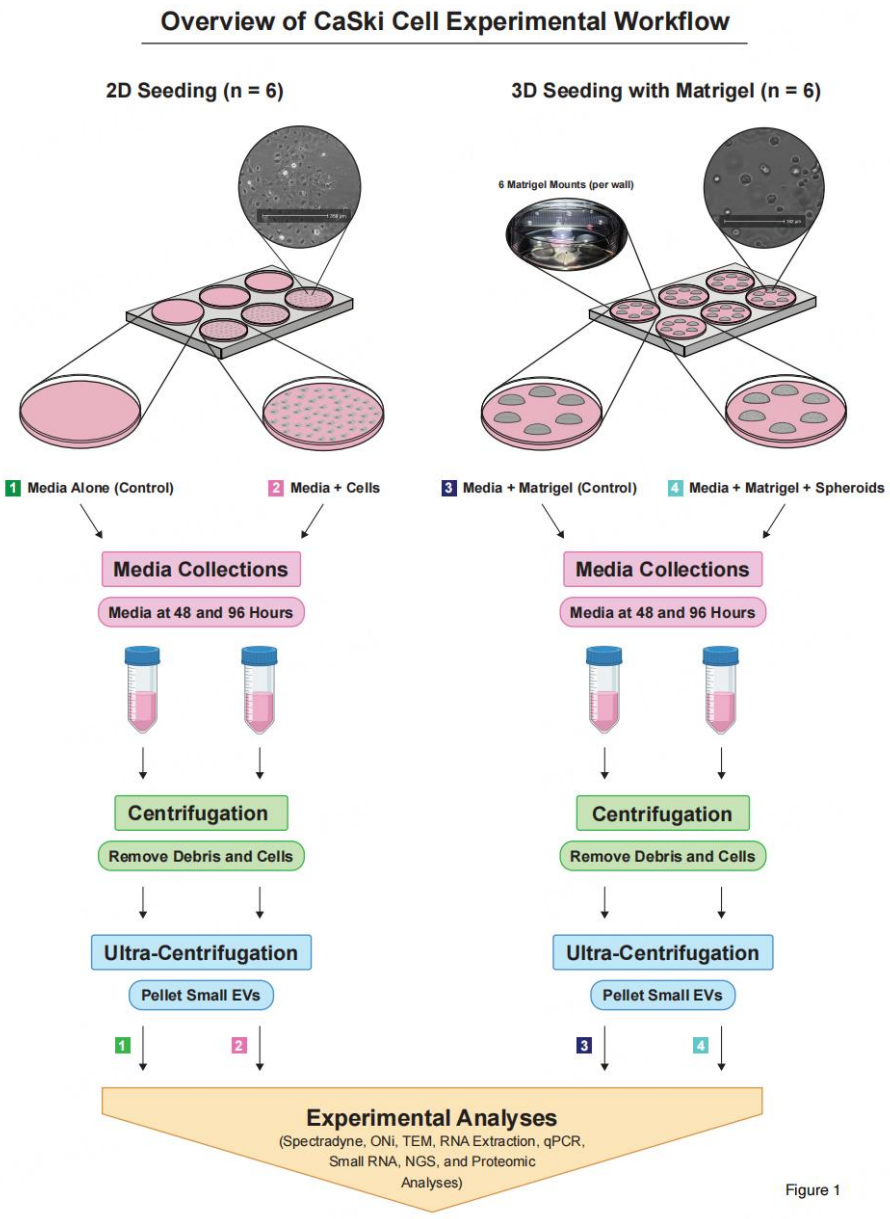


Figure 1. Experimental schematic of comparative 2-dimensional (2D) (top left) and 3-dimensional (top right) tissue culture of Ca Ski cells in 6 well-plates. For both 2D and 3D culture conditions, three wells were maintained with media alone (No cell control), and three

wells were maintained with Ca Ski cells for a total of 96 h. Pictures of the 2D and 3D cultured Ca Ski cells captured by microscope display the cells adhering flat to the bottom of 6 well plates left (2D) and in suspension in Matrigel domes (i.e., 6 domes per well). Each experimental (i.e., 2D or 3D) 6 well-plate includes 3 control wells with media only (No Cell control) and 3 experimental wells with Ca Ski cells. Both 2D and 3D size well-plates were established at the same time and maintained in tissue culture conditions for 96 h. Four different media collections (Green square for 2D media alone (No cells), Pink Square for media from Ca Ski cells maintained in 2D conditions, Dark blue square for 3D media alone (No cells), and light blue square for media from Ca Ski cells maintained in 3D conditions). For each of the four conditions, the media from three wells was collected and combined at 48 h (3× ~2 mL) and 96 h (3× ~2 mL). A total of 10 mL from each of the four different conditions was separately centrifuged to remove debris and cells, and ultracentrifuged, following a previously described procedure[45,46], generating four different pelleted samples. The ultracentrifuged pellets were resuspended in 1× PBS and underwent Spectradyne Nanoparticle Analysis, ONi Super Resolution Nanoimaging, Transmission Electron Microscopy (TEM), RNA extraction, quantitative PCR, small RNA cDNA library preparation followed by Next Generation Sequencing. The described experimental set up was repeated 6 times, to produce 6 technical replicates for the different analyses.

Analysis of small extracellular vesicles isolated from 2D and 3D culture media of Ca ski cells

To evaluate the quality of Ca Ski-derived small EVs, which were isolated by ultracentrifugation, we performed both quantitative and qualitative analyses, including Spectradyne microfluidic nanoparticle analysis, Transmission Electron Microscopy (TEM) and ONi Super-resolution nanoimaging. Nanoparticle size distribution was conducted using the Spectradyne nCS1 instrument with C-400 cartridges. Ultracentrifuged small EVs from both 2D and 3D conditioned media were analyzed, in comparison to control media samples (no cells) as baseline detection (Figure 2a, see dark blue and green plots for 2D (top panel) and 3D (bottom) media isolates). Analysis of ultracentrifuged media from Ca Ski cells cultured under 2D conditions revealed nanoparticles ranging from 60-250nm in size, consistent with the expected size range of small EVs (Figure 2a, upper panel; light red and

light blue curves representing two replicates). Equivalent analyses of culture media from Ca Ski cells cultured under 3D conditions, also confirmed the presence of nanoparticles ranging from 80-200nm in size (Figure 2a, see light red and light blue curves on bottom graph). A ~10-fold difference in nanoparticle detection was observed between media of 2D (Figure 2a, top graph see 1.7×10^{10} and 5.1×10^{10} nanoparticles) and 3D (Figure 2a, bottom graph see 2.4×10^{9} and 1.9×10^{9} nanoparticles) cultured Ca Ski cells, with control media (no cells) remaining the same for both 2D and 3D culture conditions (Figure 2a, top and bottom graph between 4.4 and 7.4 $\times$ 10^{8} nanoparticles). Comparison of nanoparticle size distribution profiles revealed a notable feature in the 3D Ca Ski-derived samples, with a distinct peak between 80-110 nm (Figure 2a, lower panel). Next, we conducted Transmission Electron Microscopy (TEM) of Ca Ski cell media isolates, from both 2D and 3D culture conditions, from two different replicates [Figure 2b]. TEM images revealed the presence of cup-shaped small extracellular vesicles (small EVs) ranging between 60-250 nm as observed for both 2D and 3D culture conditions. TEM images of Ca Ski-derived small EVs from 3D culture (Figure 2b; 4 lower panels) also revealed the presence of small EVs ranging between 60-250 nm with a noticeable peak of smaller EVs within and below 100 nm range. Having visually confirmed that the nanoparticles detected under the two different culture conditions had morphology consistent with small EVs, we then sought to validate the presence of surface tetraspanins CD9, CD63 and CD9 by conducting ONi super-resolution nanoimaging (Figure 2c; See top schematic). For these analyses we utilized the ONi human EV profiler V2 kit [Figure 2c] customized to enable the fluorescent detection of the tetraspanins CD9 (red), CD63 (blue), and CD81 (Green) on the surface of immobilized small EVs. CODI analyses revealed that single-, double-, and triple-positive immobilized small EVs could be detected in media of Ca Ski cells cultured in both 2D and 3D conditions (Figure 2c; See overall scanned grid on left and individual EVs on right, from two 2D (top four pictures) and two 3D (bottom four pictures) media isolate replicates). Collectively, these analyses confirmed that small EVs were successfully isolated by ultracentrifugation from the media of Ca Ski cells cultured under 2D conditions, as expected, but importantly also from Matrigel embedded Ca Ski 3D spheroid (Figure 1; see image of domes within six well-plates).

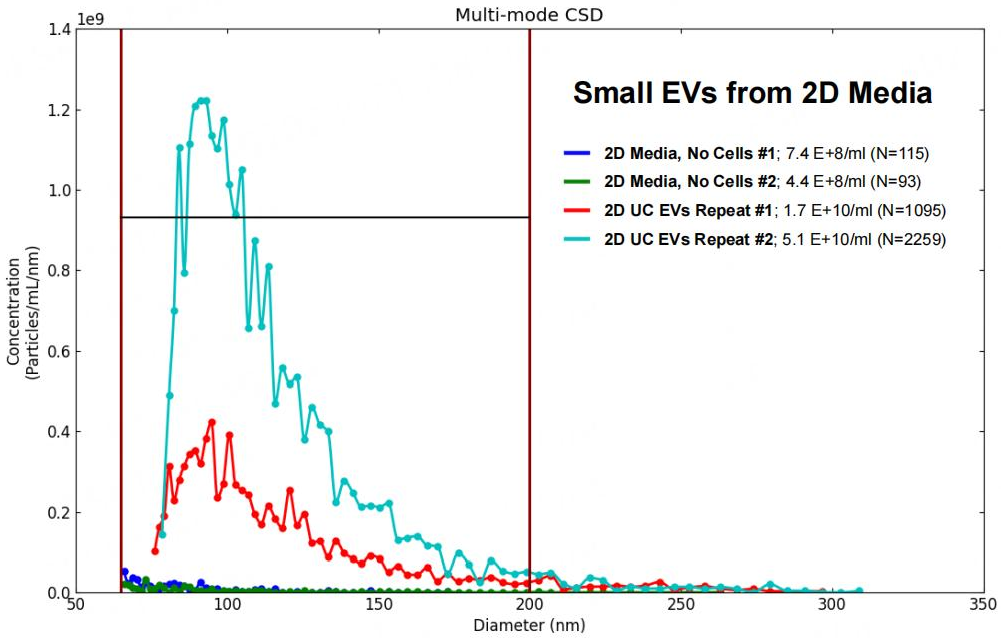
Enhanced evaluation of small extracellular vesicles isolated from 2D and 3D culture media

ONi super resolution nanoimaging enabled direct visualization of tetraspanin CD63, CD81 and CD9 proteins on the surface of immobilized small EVs as shown in Figure 2c. However, due to the high density of small EVs immobilized on the imaging grid, comprehensive evaluation of all possible small EV populations, particularly differences in tetraspanin distribution, could not be achieved globally using the ONi's CODI analysis software. Thus, we sought to perform larger-scale more robust small EV evaluations utilizing the image analysis software obtained from Nanometrix (Figure 2c; see top schematic displaying integration of the Nanometrix analysis). Using the Nanometrix software we evaluated the distribution of CD63, CD81, and CD9 on Ca Ski media-derived small EVs [Figure 2d] isolated from two biological replicates from 2D and from 3D culture conditions (See ONi glass array image at the top of Figure 2d for sample distribution). To ensure that a representative analysis of each individual lane of the ONi chip was conducted, 6 regions of interest (ROIs) were scanned per lane (i.e., per replicate). Accordingly, Nanometrix analyses were performed on a total of 12 ROIs for Ca Ski 2D media-derived small EVs (i.e., 2D replicates #1 and #2), and 12 ROIs for Ca Ski 3D media-derived small-EVs (i.e., from 3D replicates #1 and #2). The software estimated the size of the immobilized small EVs, determined the presence of CD63, CD81, and/or CD9 on individual small EVs, and re-organized them by size within single-, double-, and triple-positive small EVs lanes for 2D (left) and 3D (right) culture conditions (Figure 2d, see representative "re-organized" grids shown).

Using the "triple channel EV class analysis" in the Nanometrix software, data from 12 ROIs per condition were integrated to generate a comprehensive analysis report, including a global bar graph illustrating the relationship between small EV size and tetraspanin distribution (Figure 2d, top graphs) and a bar graph showing the overall percentages of single-, double-, and triple-tetraspanin-positive small EV populations (Figure 2d, bottom graphs). Importantly, comparison of the 2D and 3D conditions revealed changes primarily in the relative abundance of tetraspanin-defined small EV populations rather than the emergence of populations with distinct size distributions. CD63 single-positive small EVs, distributed predominantly

between 60-200 nm under both conditions, decreased from 30.9% of total small EVs under 2D conditions to 9.1% under 3D conditions [Figure 2d]. Conversely, CD81 single-positive small EVs, distributed between approximately 40-150 nm and exhibiting a pronounced peak at approximately 80 nm under both conditions, increased from 17.0% under 2D conditions to 31.8% under 3D conditions [Figure 2d]. Similarly, CD63/CD81 double-positive small EVs increased under 3D conditions, while maintaining a comparable size distribution of approximately 60-250 nm, with a peak at approximately 120 nm under both conditions [Figure 2d]. Thus, 3D culture was associated predominantly with redistribution in the relative abundance of tetraspanin-defined small EV populations rather than the generation of EV populations with new size characteristics.

a.


Multi-mode CSD
1e9
Small EVs from 2D Media
2D Media, No Cells #1; 7.4 E+8/ml (N=115)
2D Media, No Cells #2; 4.4 E+8/ml (N=93)
2D UC EVs Repeat #1; 1.7 E+10/ml (N=1095)
2D UC EVs Repeat #2; 5.1 E+10/ml (N=2259)
Concentration (Particles/mL/nm)
Diameter (nm)

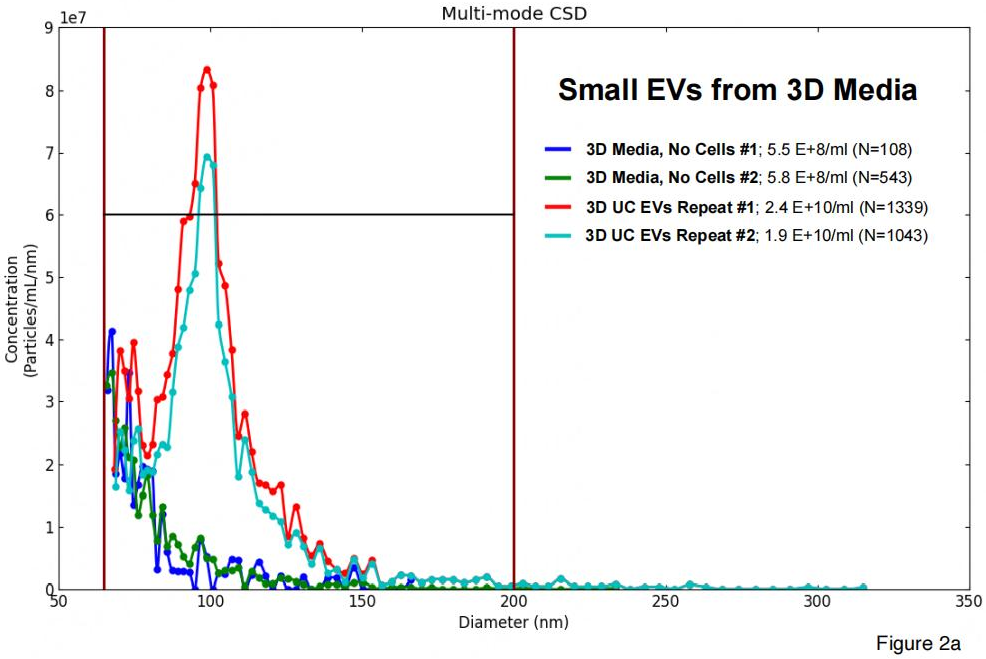

Multi-mode CSD
1e7
Small EVs from 3D Media
3D Media, No Cells #1; 5.5 E+8/ml (N=108)
3D Media, No Cells #2; 5.8 E+8/ml (N=543)
3D UC EVs Repeat #1; 2.4 E+10/ml (N=1339)
3D UC EVs Repeat #2; 1.9 E+10/ml (N=1043)
Concentration (Particles/mL/nm)
Diameter (nm)

Figure 2a

b.

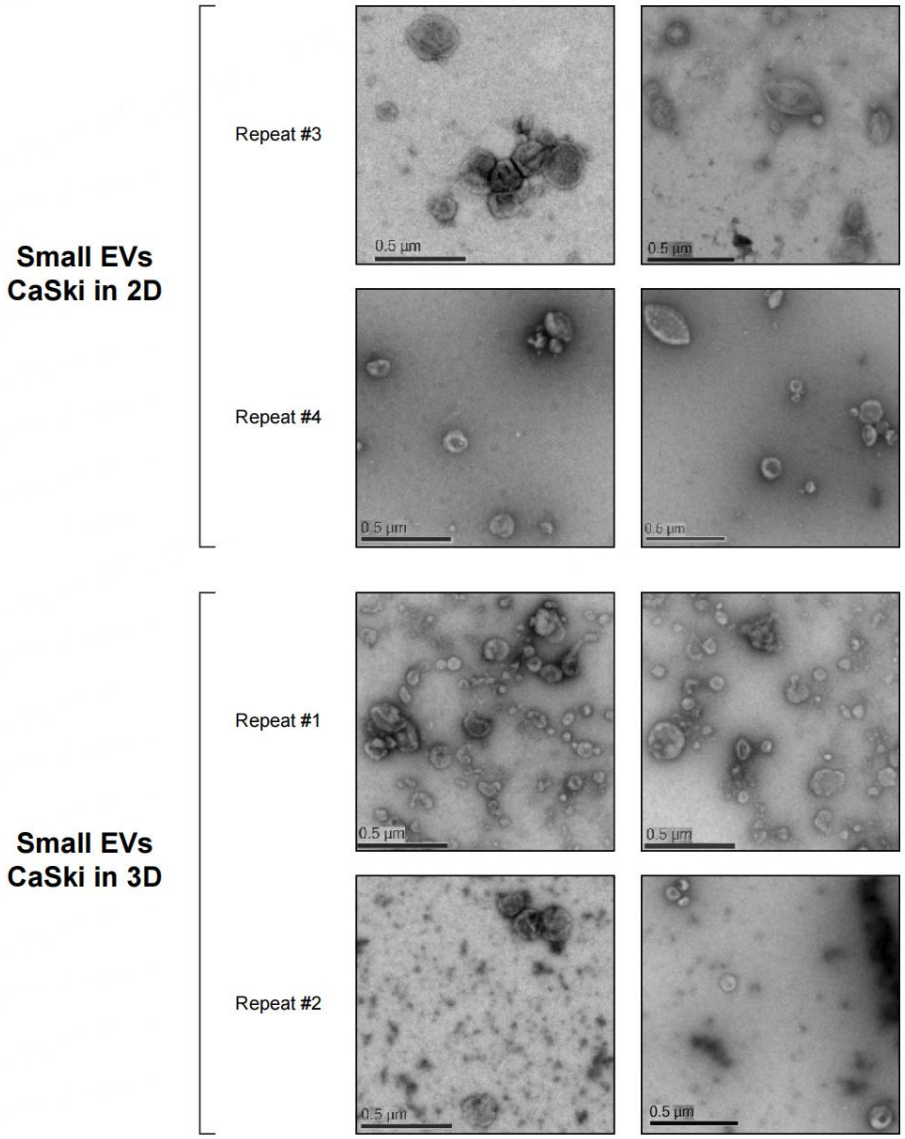
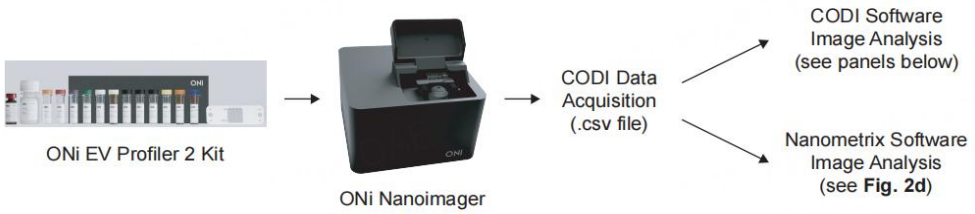

Small EVs
CaSki in 2D
Repeat #3
Repeat #4
Small EVs
CaSki in 3D
Repeat #1
Repeat #2
0.5 µm

Figure 2b

c.


ONi EV Profiler 2 Kit
ONi Nanoimager
CODI Data Acquisition (.csv file)
CODI Software Image Analysis (see panels below)
Nanometrix Software Image Analysis (see Fig. 2d)

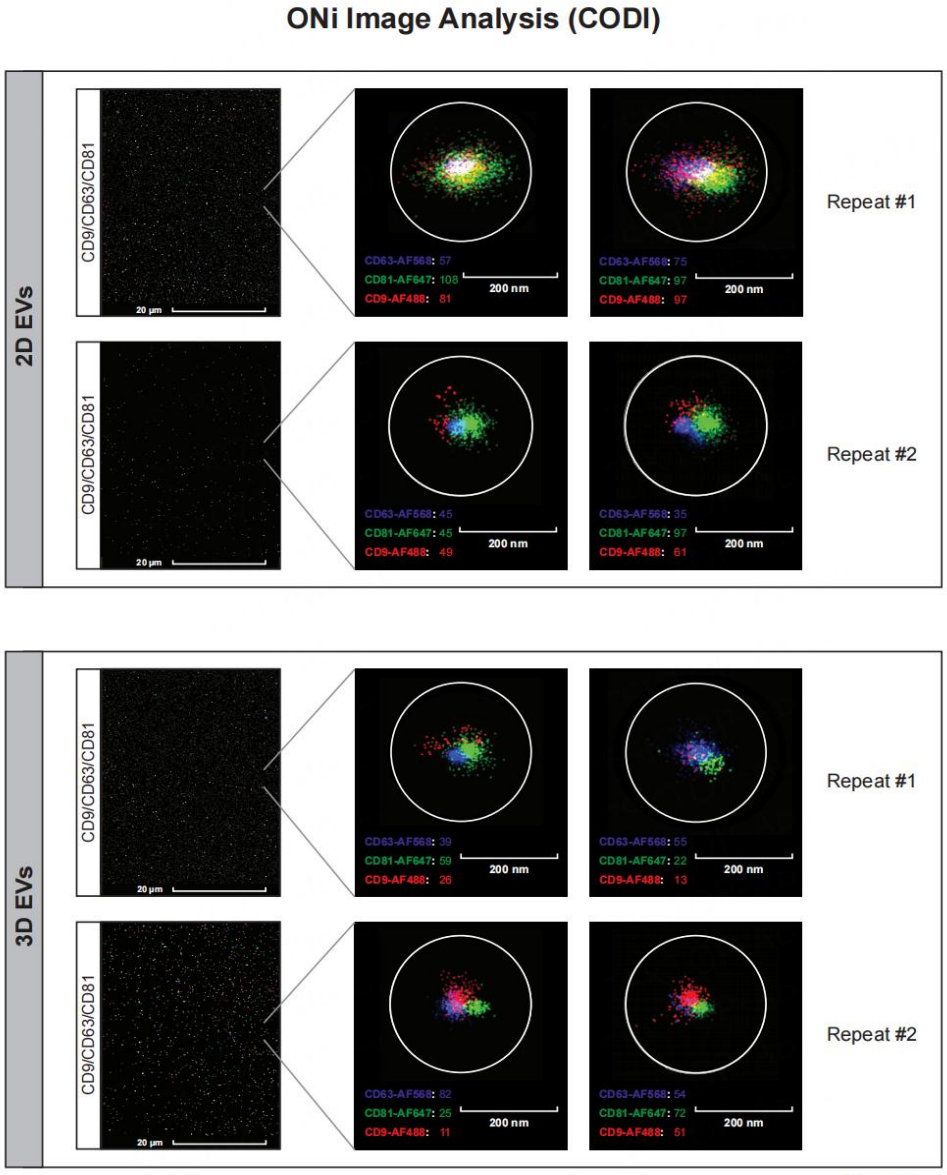

ONi Image Analysis (CODI)
2D EVs
3D EVs
CD9/CD63/CD81
Repeat #1
Repeat #2
20 µm
200 nm
CD63-AF568: 57
CD81-AF647: 108
CD9-AF488: 81
CD63-AF568: 75
CD81-AF647: 97
CD9-AF488: 97
CD63-AF568: 45
CD81-AF647: 45
CD9-AF488: 49
CD63-AF568: 35
CD81-AF647: 97
CD9-AF488: 61
CD63-AF568: 39
CD81-AF647: 59
CD9-AF488: 26
CD63-AF568: 55
CD81-AF647: 22
CD9-AF488: 13
CD63-AF568: 82
CD81-AF647: 25
CD9-AF488: 11
CD63-AF568: 54
CD81-AF647: 72
CD9-AF488: 51

Figure 2c

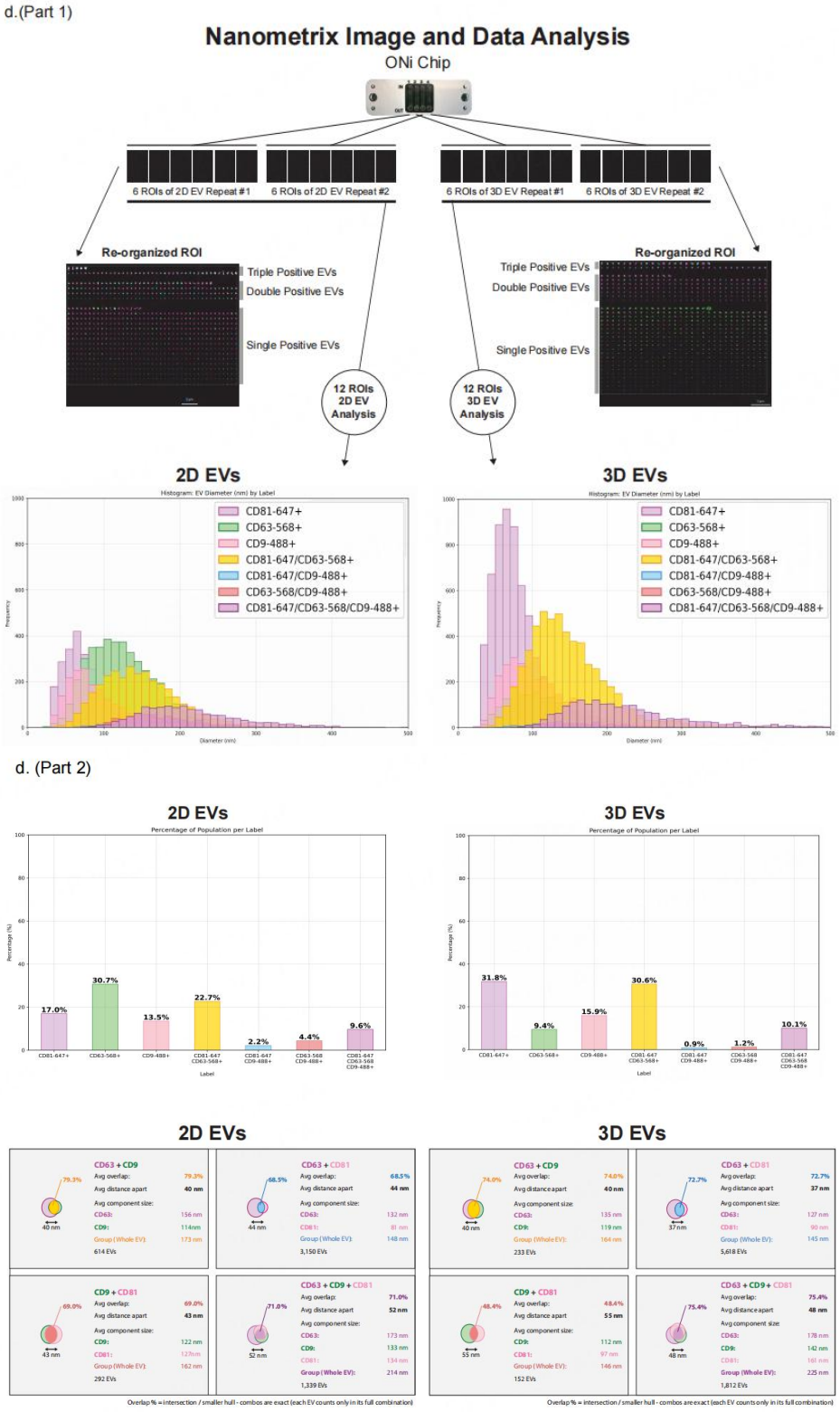


Figure 2. Analysis and validation of Ca Ski small extracellular vesicles. (a) The resuspended pellets isolated by ultracentrifugation from the media of Ca Ski cells cultured in 2D (top

graph) and 3D (bottom graph), 2D, and 3D media control without cells, for two replicates for each condition, were evaluated on C-400 microfluidic cartridges on the Spectradyne nCS1 instrument; (b) Resuspended 2D and 3D pellets obtained by ultracentrifugation from the media of cultured cells were evaluated by transmission electron microscopy (TEM). The top 4 TEM images display detection of small extracellular vesicles for two different ultracentrifuged pellets from the media of Ca Ski cells cultured in 2D conditions (i.e. 2 images side by side for each replicate, with scale bar of 0.5 mm). The bottom 4 TEM images display small extracellular vesicles detected from two different ultracentrifuged pellets from the media of Ca Ski cells cultured in 3D conditions (i.e. 2 images side by side for each replicate, with scale bar of 0.5 mm); (c) Schematic of the ONi super resolution nanoimaging for detection of CD63 (blue), CD81 (green), and CD9 (red) tetraspanins and analysis of immobilized small EVs isolated by ultracentrifugation of two 2D media replicates and two 3D media replicates. At the end of the schematic two different analytical approaches are described, including the CODI software imaging analysis provided with the ONi instrument (top), and the Nanometrix software (Independent from the ONi instrument), which was used to obtain data presented in (d) below. A large view of the ONi grid is provided for each of the two replicates for 2D small EV samples, along with two enhanced images of single small EVs for each replicate. A large view of the ONi grid is also provided for each of the two replicates for 3D small EV samples, along with two enhanced images of single small EVs, for each replicate; (d) The Nanometrix software was utilized to further evaluate the ONi imaging data. At the top of the figure an ONi chip is presented to identify the 4 lanes for each of the four samples, two for small EVs from 2D media, and 2 for small EVs from 3D media. Out of each lane a total of 6 Regions of Interest (ROIs) were acquired on the ONi instrument. For the 2D small EVs (left), 6 ROIs from each 2D small EV samples are combined for analysis (i.e., total of 12 ROIs). Similarly for the 3D small EVs (right), 6 ROIs from each of the 3D small EV samples are combined for analysis (i.e., total of 12 ROIs). The first two bar graphs represent the distribution (number of EVs) per size per single, double, and triple tetraspanin combinations (see graph legend, purple for CD81, green for CD63, pink for CD9, yellow for CD81 and CD63, blue for CD81 and CD9, orange for CD63 and CD9, and dark purple for CD81, CD63, and CD9). The lower bar graphs display the overall percentage of each type of single, double, and triple positive small EVs in percent of the total small EVs

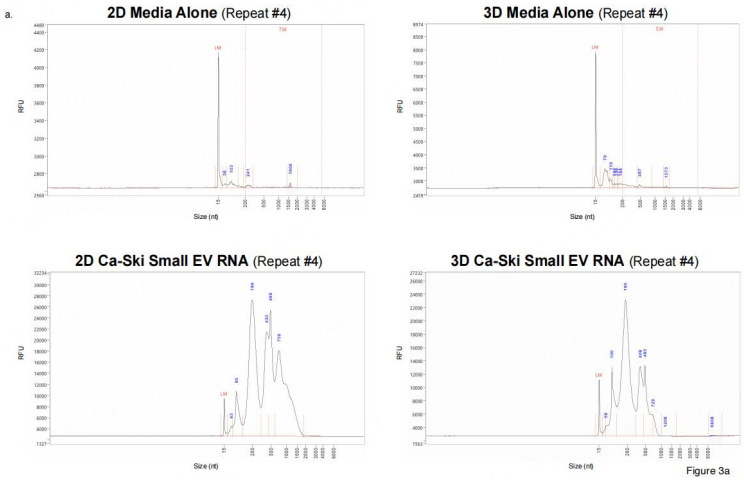
detected in the combined ROIs, regardless of size. The final lower panel illustrates tetraspanin colocalization for all double-positive combinations ($CD63^+/CD9^+$, $CD63^+/CD81^+$, and $CD9^+/CD81^+$), as well as the triple-positive ($CD9^+/CD63^+/CD81^+$) EV population. For each tetraspanin combination, the average percentage overlap, inter-marker distance, and number of positive EVs are shown, calculated from a total of 12 ROIs per group.

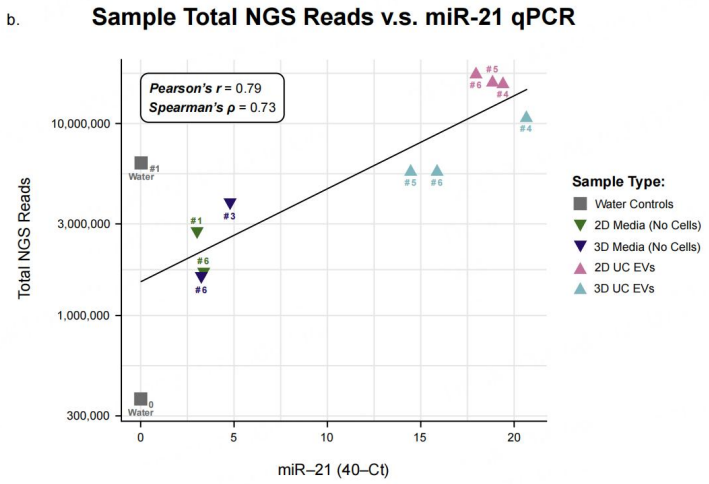
Importantly, because the same replicates (replicate #1 and replicate #2) were analyzed using both Nanometrix EV analysis software of ONi data and C-400 cartridges on the Spectradyne nCS1 instrument [Figure 2a], these datasets could be directly compared. The prominent small EV peak observed under 3D conditions using the Spectradyne platform (Figure 2, bottom graph; ~80-110 nm) corresponded closely to the size range identified by Nanometrix analysis (~50-110 nm), which predominantly comprised CD81 single-positive small EVs (Figure 2d, right bar graph; pink bars). Together, these independent analyses indicate that 3D culture alters the relative abundance of tetraspanin-defined small EV populations, with a prominent enrichment of CD81 single-positive small EVs under 3D conditions.

RNA analyses conducted on 2D and 3D small extracellular vesicles

Next, we conducted RNA extractions from the ultracentrifuged isolates obtained via our four different conditions (Figure 1, See Green, Pink, Dark blue, and light blue squares). However, given the low yield and concentration of RNA isolated (< 1ng/ l) from small EVs, we sought to quantify the abundance and evaluate the quality of small RNAs from these samples [Figure 3]. First, we obtained representative RNA profiles from our different samples using the Agilent Tapestation [Figure 3a]. Extremely small quantities of small RNAs were detected in both 2D (top left graph) and 3D (top right graph) cell-free media, with slightly higher levels observed under 3D culture conditions. Analysis of RNA isolated from small EVs derived from Ca Ski cells cultured under 2D (bottom left graph) and 3D (bottom right graph) conditions exhibited comparable small RNA peak sizes, although concentrations differed between the samples. RNA species up to 1,500 nucleotides were detected, consistent with previous reports of EV-associated RNA cargo[67]. As we expected limited amounts of RNA from our different samples, we selected miR-21 as a surrogate normalization/RNA quantity marker to comparatively assess RNA abundance and evaluate samples prior to Next

Generation Sequencing (NGS) analyses [Figure 3b]. The Ct values were calculated prior to determining fold changes, by subtracting the Ct value of each RNA samples from the averaged Ct value of RNA isolated from ultracentrifuged 2D (left bar graph) and 3D (right bar graph) media alone (Figure 1; Media no cells). miR-21 fold-change analyses revealed that RNA extracted from 2D samples demonstrated relatively uniform representation, approximately (Supplementary Figure 1, left graph, 240- to 280-fold increase compared to 2D media alone) whereas RNA extracted from 3D samples displayed lower representation (Supplementary Figure 1, right graph, 100- to 250-fold increase compared to 3D media alone) of miR-21, consistent with lower small EV representations detected by Spectradyne analyses [Figure 2a]. To determine whether miR-21 may be a useful proxy for RNA abundance, cDNA libraries were prepared from water control, ultracentrifuged 2D and 3D media without cells, and ultracentrifuged 2D and 3D Ca Ski-derived small EVs. Correlation analyses were performed between miR-21 Ct values and either total RNA reads (Supplementary Figure 2, top graph) or the total miRNA reads (Supplementary Figure 2, bottom graph). A Pearson correlation coefficient of approximately 0.79 was observed between miR-21 Ct values and total RNA reads, while a stronger correlation, $r > 0.97$, was observed between miR-21 Ct values and total miRNA reads. Collectively, these results suggest that the quantitation of miR-21 may provide a robust and reliable estimate of miRNA abundance in low-input small EV RNA samples prior to conducting NGS library preparations.





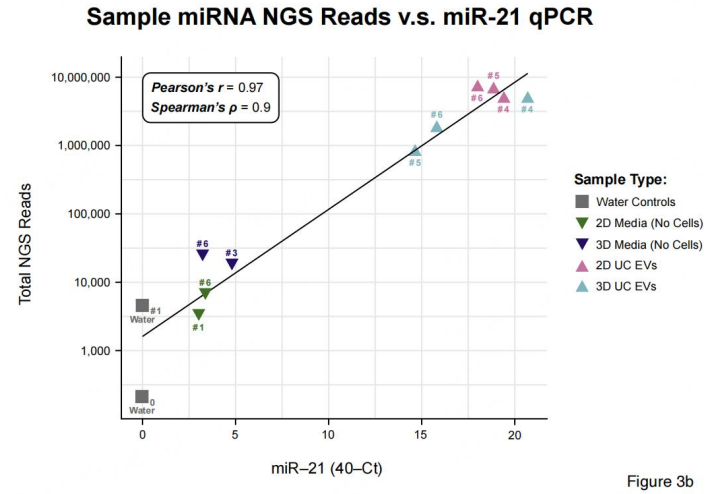


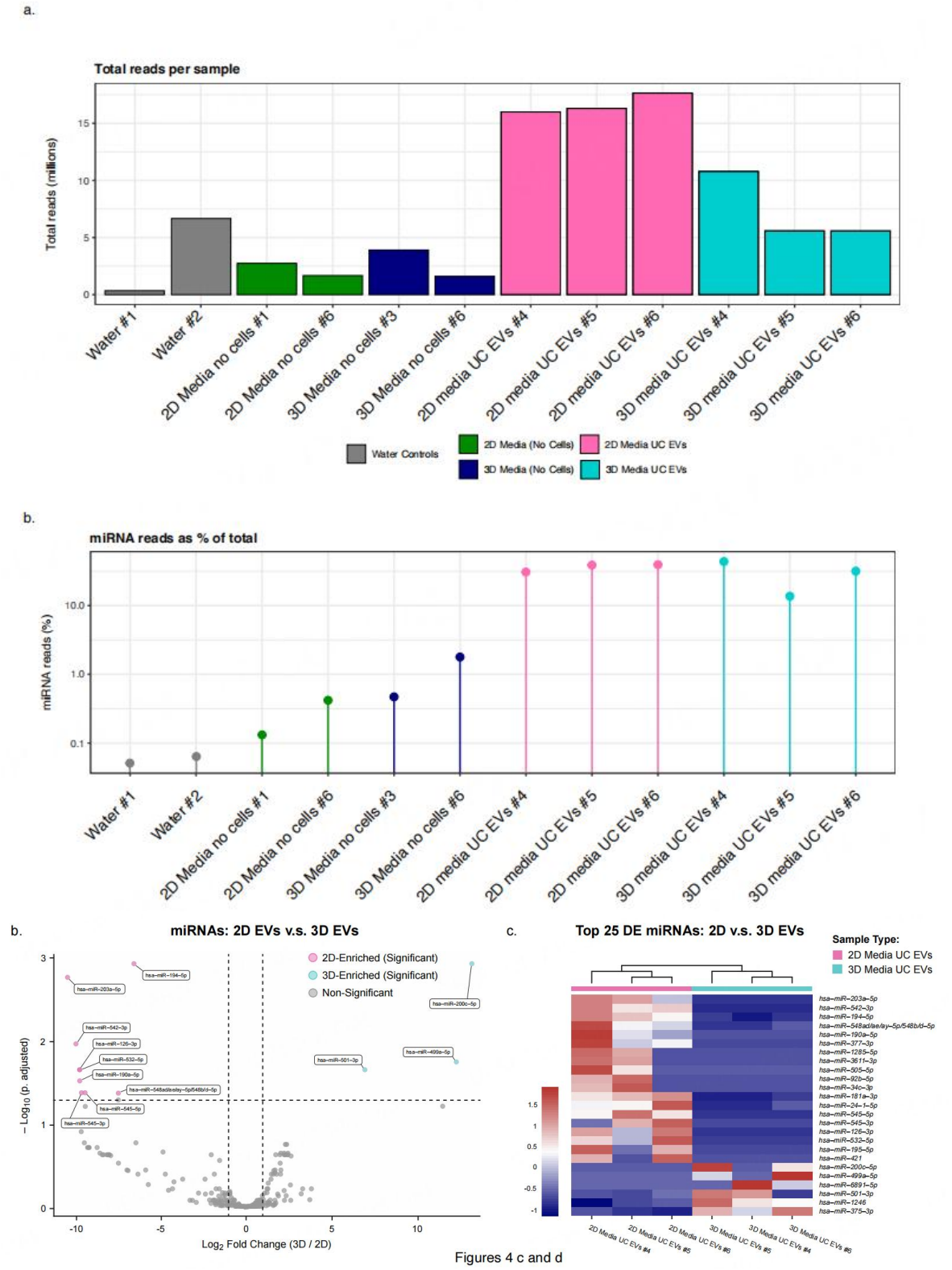
Figure 3. RNA Extraction and Quantification. (a) Agilent Tape Station analysis of total RNA extracted with the Qiagen miReasy serum/plasma kit from 4 samples (repeat#4 of 6 replicates produced for these experiments). The top two graphs display the RNA profiles of media

incubated on 3 wells of a 6 well-plate without cells (2D; top left) and media incubated on 3 wells of a 6 well-plate with Matrigel mounts without cells (3D, top right). The bottom graphs display the profile of RNA extracted from ultracentrifuged small EVs isolated from the media of cells cultured in 2D (left) and cells cultured in Matrigel mounts in 3D (right); (b) Pearson and Spearman correlation analyses of the total RNA reads (upper plot) and the total miRNA reads (lower plot) obtained by NGS analysis, for samples described in *(b)*, to their respective Ct values for miR-21. Both Pearson and Spearman values are displayed in the left corners of the plots. The samples are identified by condition, including two replicates for 2D media alone (i.e., green inverted triangles), two replicates for 3D media alone (i.e., dark blue inverted triangles), three replicates for small EVs isolated from the 2D (i.e., pink circles), and three replicates for small EVs isolated from 3D (i.e., light blue circles) media conditions. The numbers next to the triangles and circles, within the graphs, identify the sample replicates utilized for the analyses (i.e., selected from the 6 replicates prepared for this study).

Small-RNA NGS analyses of small extracellular vesicles derived from 2D and 3D media

Next, we conducted small-RNA expression analyses using Next Generation Sequencing data generated from the samples detailed in Figure 4a, including replicate water controls, replicate ultracentrifuged 2D and 3D media controls without cells, and triplicate ultracentrifuged small EVs derived from the media of Ca Ski cells cultured in 2D and 3D conditions. As depicted in the upper graph, cDNA libraries generated from small EV RNA samples yielded substantially higher read counts compared to all control samples (Figure 4a, Top bar graph, see Pink and Light blue bars). Analysis of the proportion of miRNAs relative to total NGS reads (Figure 4a, Bottom bar graph) demonstrated that small EVs derived from the media of Ca Ski cells cultured both in 2D and 3D conditions contained greater than 10% miRNA reads, representing an increase of more than 100-fold compared to water controls and more than 10-fold relative to ultracentrifuged 2D and 3D media controls without cells. We evaluated 299 miRNAs detected across all samples and visualized their differential expression using an unsupervised hierarchical clustering heatmap [Supplementary Figure 3]. The miRNA heatmap analysis demonstrated clear segregation of triplicate 2D and triplicate 3D Ca Ski derived small EV samples from all controls, and one another (Supplementary Figure 3, left). Next, we identified miRNAs that were differentially expressed between small EVs isolated

from 2D and 3D culture conditions [Figure 4]. Volcano plot analyses revealed that 12 miRNAs were significantly upregulated in 2D-derived small EVs (Figure 4a, see pink red dots; miR-194-5p, miR-203a-5p, miR-542-3p, miR-126-3p, miR-190a-5p, miR-545-5p, miR-545-3p, miR-548ad-5p, miR548ae-5p, miR548ay-5p, miR-548b-5p, miR-548d-5p), whereas only three miRNAs were significantly enriched in 3D-derived small EVs (Figure 4a, see light blue dots; miR-200c-5p, miR-499a-5p, and miR-501-3p). To further evaluate reproducible detection between replicates, we examined the top 25 differentially expressed miRNAs based on read counts [Figure 4c]. We determined that 19 of these miRNAs were reproducibly upregulated in 2D-derived small EVs, whereas only 6 were enriched in 3D-derived small EVs. A similar pattern was observed for tRFs (Figure 5b, bottom left heatmap), with 20 of the top 25 transcripts preferentially upregulated in 2D-derived small EVs and only 5 upregulated in 3D-derived small EVs. Given that tRNA-derived fragments (tRFs), like miRNAs, are implicated in the regulation of post-transcriptional gene expression and that they have been detected in small EVs[68], we evaluated the 188 tRFs detected across the samples and similarly represented their differential expression using an unsupervised hierarchical clustering heatmap (Supplementary Figure 3, right). Although the tRF heatmap analyses distinguished small EV samples from controls, it showed less differences between 2D and 3D conditions than that seen for the miRNAs, likely reflecting the lower abundance of tRFs detected in our small EV RNA extracts. However, differential expression analysis of tRFs identified 8 transcripts significantly upregulated in 2D small EVs (Supplementary Figure 4, see pink dots) and only 2 significantly upregulated in 3D small EVs (Supplementary Figure 4, see light blue dots). In both miRNAs and tRF analyses, a larger number of transcripts appeared to be preferentially expressed in 2D-derived compared with 3D-derived small EVs. Collectively, these results suggest that while 3D Matrigel-based culture does not prevent the diffusion of small EVs into conditioned media, our analyses reveal that the small RNA cargo profiles differ between 2D and 3D culture conditions, with broader enrichment of detectable miRNAs and tRFs observed in 2D Ca Ski-derived small EVs.



Figures 4 c and d

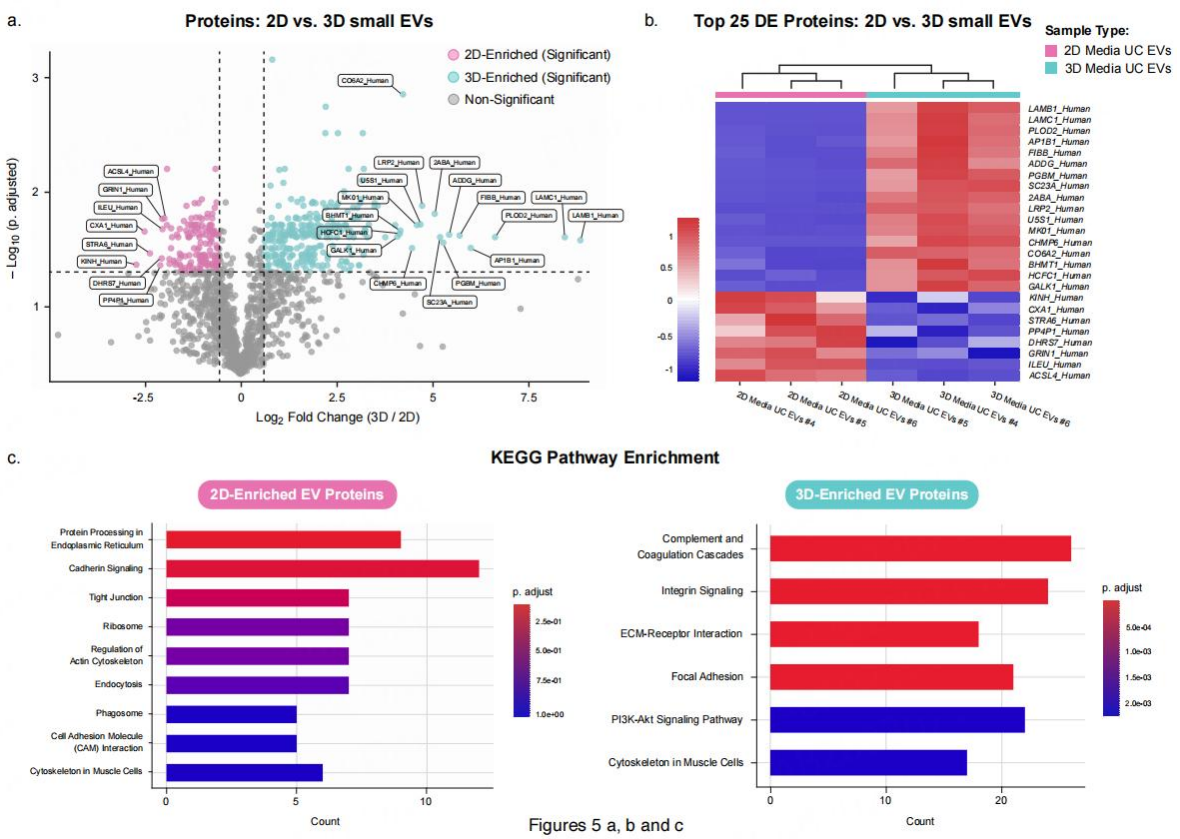
Figure 4. Differential miRNA profiling of small EVs derived from 2D and 3D Ca Ski cell cultures. (a) The top bar graph displays the total number of read per sample sequenced,

including RNA extracts from water #1 and #2 (grey), 2D media without cells #1 and #2 (green), 3D media without cells #1 and #2 (blue), ultracentrifuged small EVs from 2D media #1 and #2 (pink), and ultracentrifuged small EVs from 3D media #1 and #2 (light blue) as displayed on the x-axis. The y-axis displays the total number of reads in millions per library; (b) The bar graph displays the percentage of microRNAs per library on the y-axis, for RNA extracts from water #1 and #2 (grey), 2D media without cells #1 and #2 (green), 3D media without cells #1 and #2 (blue), ultracentrifuged small EVs from 2D media #1 and #2 (pink), and ultracentrifuged small EVs from 3D media #1 and #2 (light blue), on the x-axis; (c) Volcano plot of miRNAs differentially expressed between small EVs isolated from 2D and 3D cell culture media. Teal nodes indicate miRNAs significantly enriched in 3D EVs, pink nodes indicate miRNAs significantly enriched in 2D EVs, and gray nodes indicate non-significant transcripts. Labels identify individual differentially expressed miRNAs; (d) Heatmap of the top 25 differentially expressed miRNAs isolated from 2D (pink) and 3D (teal) culture media. miRNA expression is displayed as z-score-normalized values, with blue indicating relatively lower expression and red indicating relatively higher expression. The color scale is shown to the left of the heatmap, and miRNA names are listed to the right.

Differential proteomic analyses between 2D and 3D media-derived small EVs

Next, we conducted mass spectrometry-based proteomic analyses of small EVs isolated from 2D and 3D culture media. The three biological replicates from each culture condition clustered exclusively according to culture condition, with minimal overlap between 2D- and 3D-derived EVs, supporting the high reproducibility of the proteomic measurements [Supplementary Figure 4]. An average of close to 2,000 proteins was detected per sample. Across the two culture conditions, 422 proteins were differentially expressed. Volcano plot analysis [Figure 5a] identified 281 proteins significantly enriched in 3D-derived small EVs (66.6%), whereas 141 proteins were significantly enriched in 2D-derived small EVs (33.4%). Consistent with these findings, hierarchical clustering of the 25 most differentially expressed proteins, comprising seventeen 3D-enriched and eight 2D-enriched proteins, clearly separated the EV samples according to culture condition and further highlighted high reproducibility between the proteomic profiles as well as the applicability of protocol[56] for small EV protein identification [Figure 5b]. We next performed separate KEGG pathway

enrichment analyses for the 141 and 281 proteins enriched in 2D- and 3D-derived small EVs, respectively [Figure 5c]. The two EV populations exhibited distinct functional enrichment patterns, indicating that culture dimensionality substantially influences the molecular composition and functional characteristics of EVs released by Ca Ski cells. Proteins enriched in 2D-derived EVs were associated primarily with protein processing in the endoplasmic reticulum, cadherin signaling, tight junctions, ribosome, actin cytoskeleton regulation, endocytosis, and phagosome-related pathways. In contrast, 3D-derived EV proteins showed strong enrichment for complement and coagulation cascades, integrin signaling, ECM-receptor interaction, focal adhesion, PI3K-Akt signaling, and cytoskeletal pathways, suggesting a distinct EV-associated molecular program characteristic of the three-dimensional culture environment.



Figures 5 a, b and c

Figure 5. Differential proteomics profiling and KEGG pathway enrichment of small EVs derived from 2D and 3D Ca Ski cell cultures. (a) Volcano plot of proteins differentially expressed between small EVs isolated from 2D and 3D cell culture media. Teal nodes indicate proteins significantly enriched in 3D EVs, pink nodes indicate proteins significantly

enriched in 2D EVs, and gray nodes indicate non-significant proteins. Labels identify individual differentially expressed proteins; (b) Heatmap of the top 25 differentially expressed proteins in small EVs isolated from 2D (pink) and 3D (teal) culture media. Protein abundance is displayed as z-score-normalized values, with blue indicating relative lower abundance and red indicating relative higher abundance. The color scale is shown to the left of the heatmap, and protein names are listed to the right; (c) KEGG pathway enrichment analysis of biological pathways associated with differentially expressed small EV proteins between 2D and 3D culture conditions. Bar charts display the top enriched pathways among 2D-enriched EV proteins (left) and 3D-enriched EV proteins (right). Pathways are plotted by gene count and colored according to statistical significance ($-\log_{10}$ adjusted *p*-value), with separate color scales shown to the right of each panel.

Finally, to examine whether the differences observed between 2D- and 3D-derived EVs at the protein level were functionally related to the small-RNA differences identified above, we performed KEGG pathway analysis of predicted targets of miRNAs enriched in 2D-derived EVs and compared these pathways with those enriched among proteins identified in 3D-derived EVs [Figure 6]. Given the loss of specific miRNAs in 3D-derived small EVs, we hypothesized that their predicted targets may be less negatively regulated and consequently enriched among proteins detected in 3D-derived EVs. Notably, several pathways enriched among 3D-derived EV proteins, including integrin signaling, focal adhesion, ECM-receptor interaction, PI3K-Akt signaling, and cytoskeletal regulation, were also enriched among the predicted targets of miRNAs that were only upregulated in 2D-derived small EVs. Thus, the pathways enriched among 3D-derived EV proteins contained multiple predicted targets of miRNAs that were preferentially present in 2D-derived small EVs but then downregulated in 3D-derived EVs.

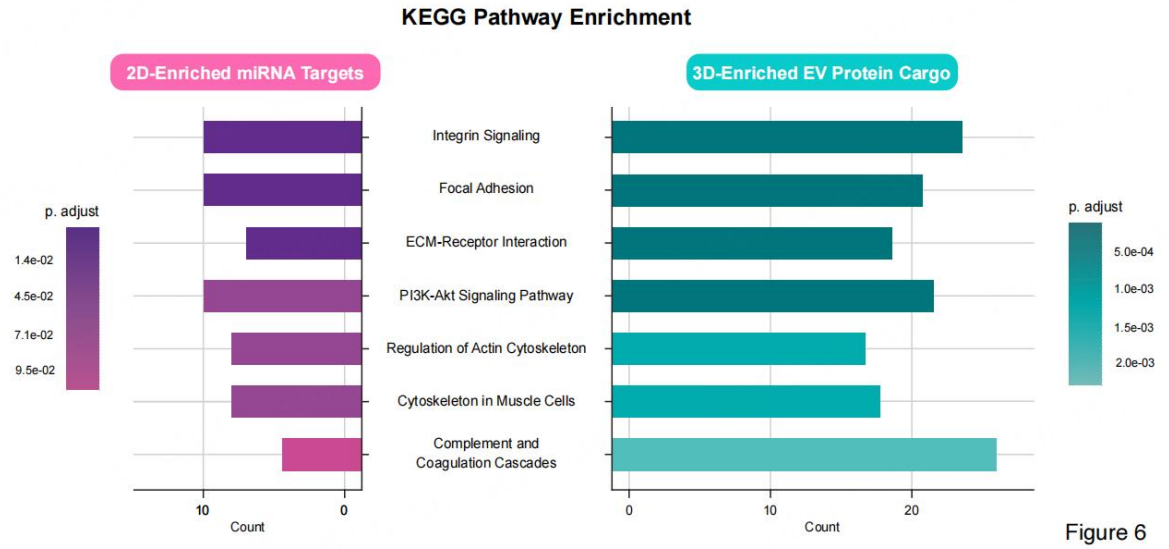


Figure 6. Comparative KEGG pathway enrichment of 2D EV miRNA targets and 3D EV proteins. Comparative KEGG pathway enrichment analysis integrating predicted targets of 2D-enriched miRNAs with identified 3D-enriched EV cargo proteins. Predicted mRNA targets of 2D-enriched miRNAs (retrieved via miRWalk) were cross-referenced against 3D-enriched EV proteins to identify overlapping target genes. The dual bar chart displays top shared functional biological pathways enriched among predicted 2D-miRNA targets (left panel) and actual 3D EV proteins (right panel). Pathways are plotted by gene count and colored by statistical significance (-$\log_{10}$ adjusted *p*-value), with distinct color scale bars displayed for each panel.

DISCUSSION

In this study, we characterized small extracellular vesicles (small EVs) released by Ca Ski cervical cancer cells under conventional two-dimensional (2D) monolayer and three-dimensional (3D) Matrigel-embedded spheroid conditions. Using complementary physical characterization methods, including Spectradyne nanoparticle analysis, transmission electron microscopy (TEM), and ONi super-resolution nanoimaging, together with small RNA next-generation sequencing (NGS) and data-independent acquisition mass spectrometry (DIA-MS), we demonstrated that small EV populations generated under these two culture conditions differ substantially in particle abundance and size distribution, surface tetraspanin composition, and small-RNA and protein cargo. These findings indicate that the culture environment in which tumor cells are maintained can influence the characteristics and

molecular cargo of the small EV populations they release. Importantly, despite the reduced abundance of small EVs recovered from 3D cultures, sufficient material was reproducibly obtained from Matrigel-embedded spheroids for downstream molecular characterization. Together, these findings support the use of 3D culture models as a feasible experimental system for investigating tumor cell-derived small EVs and establish the technical feasibility needed for future studies using patient-derived cervical tumor organoids.

As a first step in evaluating the suitability of 3D culture for small EV studies, we compared monoclonal Ca Ski cells grown as Matrigel-embedded spheroids with conventional 2D monolayer cultures. Small EVs were reproducibly isolated from only 10 mL of 3D-conditioned media and characterized by nanoparticle analysis, TEM, and ONi super-resolution nanoimaging. Recovered EV material was sufficient for qPCR and small RNA NGS, with minimal background RNA from cell-free 3D culture medium, as well as sensitive proteomic characterization by DIA-MS. These findings establish the feasibility of molecularly profiling small EVs from limited volumes of 3D-conditioned media.

Given that small EVs comprise heterogeneous populations that differ in size, molecular composition, and biogenesis pathways[69-71], and that cellular architecture and culture conditions can alter their miRNA and protein cargo[42,43], we first investigated whether physical differences between small EVs generated under matched 2D and 3D conditions could be observed. Topology-guided, AI-assisted Nanometrix analysis of ONi super-resolution imaging datasets revealed marked shifts in the composition of small EV populations between 2D and 3D culture conditions. CD81 single-positive small EVs, predominantly distributed between 30 and 100 nm under both conditions, increased from 17.1% of the population under 2D conditions to 31.8% under 3D conditions. Notably, independent Spectradyne nanoparticle analysis identified a prominent 80-110 nm population in 3D-derived small EVs, closely corresponding to the size distribution of the CD81 single-positive population resolved by ONi/Nanometrix analysis. CD63/CD81 double-positive EVs, which ranged from approximately 50 to 200 nm under both conditions, were also proportionally enriched under 3D conditions (30.6% versus 22.7% under 2D conditions). In contrast, CD63 single-positive EVs, which ranged from approximately 50 to 200 nm, were

substantially more abundant under 2D conditions (30.9% versus 9.1% under 3D conditions). Interestingly, although specific small EV subpopulations were proportionally enriched under 3D conditions, approximately ten-fold fewer nanoparticles were recovered from conditioned medium of Matrigel-embedded spheroids despite seeding identical numbers of cells under both conditions. This reduction may reflect retention of secreted small EVs within the Matrigel matrix and/or differences in cell growth, EV production, or secretion under 3D conditions. Consistent with our observations, Thippabhotla *et al.* (2019) reported altered EV secretion and particle-size distributions following transition of cervical cancer cells from 2D to 3D culture[72]. Although their quantitative findings differed from ours, both studies indicate that EV output and physical characteristics are influenced by culture conditions. The altered CD63/CD81 distributions are also consistent with evidence that these canonical tetraspanins can define partially overlapping but molecularly distinct EV subpopulations[72-74] and exhibit distinct intracellular trafficking behaviors. CD63 undergoes constitutive endocytosis and endolysosomal trafficking, whereas CD81 is predominantly localized at the plasma membrane, and perturbation of endocytic trafficking can selectively alter CD63 vesicular secretion without similarly affecting CD81[73]. Together with the known influence of ESCRT-dependent and -independent pathways, lipid microdomains, and cellular context on EV biogenesis[75,76], these differences provide a potential biological context for the altered CD63- and CD81-positive EV populations observed under 3D conditions, although the underlying mechanisms remain to be determined.

Relatively few studies have directly compared the small RNA and protein cargo of small EVs produced by the same cancer cell line under matched 2D and 3D conditions. We first conducted side-by-side small RNA NGS profiling of small EVs from both conditions, including water, cell-free culture medium, and medium incubated with Matrigel in the absence of cells as controls[54,77]. Cell-free medium yielded modest read counts, with slightly higher RNA and small RNA levels in Matrigel-containing medium; however, these background signals remained low relative to Ca Ski-derived small EVs and did not interfere with downstream analyses. Given the low amount of small EV RNA recovered from 10 mL of conditioned medium, we quantified miR-21 by qPCR to normalize RNA input before NGS library preparation. miR-21 was negligible in cell-free controls (Ct 33-38), while its levels in

EV samples strongly correlated with subsequent total ($r > 0.79$) and miRNA ($r > 0.97$) read counts, supporting its use as a practical measure for normalizing small EV RNA input prior to NGS.

Small RNA profiling revealed reproducible differences in EV-associated miRNAs and tRNA-derived fragments (tRFs) between 2D and 3D culture conditions, with principal component analysis separating both EV populations from controls. MiRNAs comprised more than 10% of total sequencing reads in small EV libraries, representing more than 100-fold enrichment relative to water controls, and a greater number of miRNAs were more abundant in 2D- than 3D-derived small EVs. We therefore examined whether this pattern extended to tRFs, which have emerged as regulators of gene expression and cellular stress responses and have been detected in EVs across diverse biological systems[78-84]. Although tRF profiles clearly distinguished EV samples from controls, differences between 2D- and 3D-derived EVs were less pronounced than for miRNAs, possibly reflecting their lower relative abundance. Nevertheless, a substantial proportion of tRFs also showed lower abundance in 3D-derived EVs. Consistent with our findings, Thippabhotla *et al.* (2019) reported differences in EV miRNA profiles between cervical cancer cells maintained under 2D and 3D conditions and, notably, found that 3D-derived EV profiles showed greater similarity to circulating EVs from cervical cancer patient plasma[72]. Our findings extend these observations to tRFs, indicating that culture-dependent differences encompass multiple classes of EV-associated small RNAs.

Next, we investigated whether 2D and 3D culture conditions similarly influenced the protein cargo of Ca Ski-derived small EVs using a highly sensitive proteomic workflow that we previously developed and validated[56,57]. Triplicate analyses identified up to 1,979 proteins per sample, of which 422 were significantly differentially expressed, with approximately twice as many enriched in 3D- as in 2D-derived small EVs (281 versus 141, respectively). Given the inhibitory role of miRNAs in regulating gene expression, we examined whether these protein differences exhibited functional relationships with the differentially represented miRNAs. Integration of the two datasets revealed an inverse pathway-level relationship, whereby pathways predicted to be targeted by miRNAs enriched in 2D-derived small EVs

overlapped with those represented among proteins enriched in 3D-derived small EVs. This relationship was particularly evident for pathways associated with extracellular matrix interactions, tight junctions, cell adhesion, focal adhesion, PI3K-Akt signaling, and cytoskeletal organization. Although these findings do not establish direct regulatory relationships between EV-associated miRNAs and proteins, they demonstrate that differences in small RNA and protein cargo between 2D- and 3D-derived small EVs converge at the pathway level on biological processes related to cellular architecture and interactions with the extracellular environment.

Technically, 3D spheroid cultures generated sufficient small EVs for molecular characterization from approximately three million Ca Ski cells using as little as 10 mL of conditioned medium collected at 48 and 96 h post-seeding. Given that 3D culture incorporates aspects of cellular architecture and extracellular matrix interactions absent from conventional 2D monolayers[85-87], the differences observed in small EV populations and molecular cargo highlight the importance of culture context when generating EV datasets for biomarker discovery. Reliance solely on 2D-derived small EVs may therefore overlook vesicle populations or molecular signatures associated with three-dimensional growth. Collectively, our findings demonstrate that 3D tumor cell culture provides a useful experimental platform for investigating small EV composition and establish a technical foundation for extending these analyses to patient-derived cervical tumor organoid models.

DECLARATIONS

Financial support and sponsorship

We thank the Susan Zabransky Foundation for Cervical Cancer Research for providing funds that enabled the design of this study. The timsTOF Ultra II coupled to nanoElute 2 system and related proteomics work were in part supported by NIH P30 CA051008 and NIH S10OD028623. We also thank Dr. Thomas Tuschl, head of the Laboratory for RNA Molecular Biology at Rockefeller, for allowing access to the RNAworld pipeline.

Conflict of interest

Dr. Olivier Loudig and Dr. Megan Mitchell disclose that they have financial interests in EValuate Diagnostics, Inc., a company established for the identification of disease biomarkers.

Copyright

© The Author(s) 2026.

REFERENCES

1. Siegel RL, Miller KD, Jemal A. Cancer statistics, 2024. *CA Cancer J Clin.* 2024;74:17-48.[DOI: 10.3322/caac.21820]

2. American Cancer Society. Cancer Facts & Figures 2024. *Atlanta: American Cancer Society;* 2024.https://www.cancer.org/research/cancer-facts-statistics/all-cancer-facts-figures/2024-cancer-facts-figures.html

3. Benard VB, Watson M, Castle PE, Saraiya M. Cervical carcinoma rates among young females in the United States. *Obstet Gynecol.* 2012;120:1117-23.[PMID: 23090530 PMCID: PMC4540330 DOI: 10.1097/aog.0b013e31826e4609]

4. Buskwofie A, David-West G, Clare CA. A review of cervical cancer: incidence and disparities. *J Natl Med Assoc.* 2020;112:229-32.[PMID: 32278478 DOI: 10.1016/j.jnma.2020.03.002]

5. Walboomers JMM, Jacobs MV, Manos MM, et al. Human papillomavirus is a necessary cause of invasive cervical cancer worldwide. *J Pathol.* 1999;189:12-9.[PMID: 10451482 DOI: 10.1002/(SICI)1096-9896(199909)189:1<12::AID-PATH431>3.0.CO;2-F]

6. Schiffman M, Castle PE, Jeronimo J, Rodriguez AC, Wacholder S. Human papillomavirus and cervical cancer. *Lancet.* 2007;370:890-907.[PMID: 31500479 PMCID: PMC7062568 DOI: 10.1080/01443615.2019.1634030]

7. Perkins RB, Guido RS, Castle PE, et al. 2019 ASCCP risk-based management consensus guidelines. *J Low Genit Tract Dis.* 2020;24:102-31.[PMID: 32243307 PMCID: PMC7147428 DOI: 10.1097/LGT.0000000000000525]

8. SEER Program (National Cancer Institute). Cervical cancer survival statistics. https://seer.cancer.gov

9. Kalluri R, LeBleu VS. The biology, function, and biomedical applications of extracellular vesicles. *Science.* 2020;367:eaau6977.[PMID: 32029601 PMCID: PMC7717626 DOI: 10.1126/science.aau6977]

10. Yáñez-Mó M, Siljander PR-M, Andreu Z, et al. Biological properties of extracellular vesicles. *J Extracell Vesicles.* 2015;4:27066.[DOI: 10.3402/jev.v4.27066]

11. Mitchell PS, Parkin RK, Kroh EM, et al. Circulating microRNAs as stable blood-based markers for cancer detection. *Proc Natl Acad Sci USA.* 2008;105:10513-8.[PMID: 18663219 PMCID: PMC2492472 DOI: 10.1073/pnas.0804549105]

12. Zhou X, Wen W, Shan X, et al. A six-microRNA panel in serum as a biomarker for cervical cancer. *Cancer Prev Res.* 2015;8:36-45.[DOI: 10.18632/oncotarget.14311]

13. Huang X, Yuan T, Liang M, et al. Exosomal miR-1290 and miR-375 as prognostic markers in cancer. *Clin Cancer Res.* 2015;21:412-23.[PMID: 25129854 PMCID: PMC4252606 DOI: 10.1016/j.eururo.2014.07.035]

14. Théry C, Zitvogel L, Amigorena S. Exosomes: composition, biogenesis and function. *Nat Rev Immunol.* 2002;2:569-79.[PMID: 12154376 DOI: 10.1038/nri855]

15. Raposo G, Stoorvogel W. Extracellular vesicles: exosomes, microvesicles, and friends. *J Cell Biol.* 2013;200:373-83.[PMID: 12154376 DOI: 10.1038/nri855]

16. van Niel G, D'Angelo G, Raposo G. Shedding light on the cell biology of extracellular vesicles. *Nat Rev Mol Cell Biol.* 2018;19:213-28.[PMID: 29339798 DOI: 10.1038/nrm.2017.125]

17. Bartel DP. MicroRNAs: genomics, biogenesis, mechanism, and function. *Cell.* 2004;116:281-97.[PMID: 14744438 DOI: 10.1016/s0092-8674(04)00045-5]

18. O'Brien J, Hayder H, Zayed Y, Peng C. Overview of microRNA biogenesis, mechanisms of actions, and circulation. *Front Endocrinol.* 2018;9:402.[PMID: 30123182 PMCID: PMC6085463 DOI: 10.3389/fendo.2018.00402]

19. Li Y, Sui S, Goel A. Extracellular vesicles associated microRNAs: Their biology and clinical significance as biomarkers in gastrointestinal cancers. *Semin Cancer Biol.* 2024 Feb;99:5-23.[DOI: 10.1016/j.semcancer.2024.02.001. Epub 2024 Feb 9. PMID: 38341121; PMCID: PMC11774199]

20. Squadrito mL, Baer C, Burdet F, et al. Endogenous RNAs modulate microRNA sorting to exosomes. *Cell Rep.* 2014;8:1432-46.[PMID: 25159140 DOI: 10.1016/j.celrep.2014.07.035]

21. Chevillet JR, Kang Q, Ruf IK, et al. Quantitative and stoichiometric analysis of the microRNA content of exosomes. *Proc Natl Acad Sci USA*. 2014;111:14888-93.[PMID: 25267620 PMCID: PMC4205618 DOI: 10.1073/pnas.1408301111]

22. Wei Z, Batagov AO, Carter DRF, Krichevsky AM. Fetal bovine serum RNA interferes with the cell culture derived extracellular RNA. *Sci Rep.* 2016;6:31175.[PMID: 27503761 PMCID: PMC4977539 DOI: 10.1038/srep31175

23. Valadi H, Ekström K, Bossios A, et al. Exosome-mediated transfer of mRNAs and microRNAs is a novel mechanism of genetic exchange between cells. *Nat Cell Biol.* 2007;9:654-9.[PMID: 17486113 DOI: 10.1038/ncb1596]

24. Schwarzenbach H, Nishida N, Calin GA, Pantel K. Clinical relevance of circulating cell-free microRNAs in cancer. *Nat Rev Clin Oncol.* 2014;11:145-56.[PMID: 24492836 DOI: 10.1038/nrclinonc.2014.5]

25. Kosaka N, Iguchi H, Ochiya T. Circulating microRNA in body fluid: a new potential biomarker for cancer diagnosis and prognosis. *Cancer Sci.* 2010;101:2087-92.[PMID: 20624164 PMCID: PMC11159200 DOI: 10.1111/j.1349-7006.2010.01650.x]

26. Winn-Deen ES, Bortolin LT, Gusenleitner D, et al. Improving Specificity for Ovarian Cancer Screening Using a Novel Extracellular Vesicle-Based Blood Test: Performance in a Training and Verification Cohort. *J Mol Diagn.* 2024 Dec;26(12):1129-48.[DOI: 10.1016/j.jmoldx.2024.09.001. Epub 2024 Sep 24. PMID: 39326669; PMCID: PMC11600309]

27. Salem DP, Bortolin LT, Gusenleitner D, et al. Colocalization of Cancer-Associated Biomarkers on Single Extracellular Vesicles for Early Detection of Cancer. *J Mol Diagn.* 2024 Dec;26(12):1109-28.[DOI: 10.1016/j.jmoldx.2024.08.006. Epub 2024 Sep 24. PMID: 39326670; PMCID: PMC13169315]

28.Villarroya-Beltri C, Gutiérrez-Vázquez C, Sánchez-Cabo F, et al. Sumoylated hnRNPA2B1 controls the sorting of miRNAs into exosomes. *Nat Commun.* 2013;4:2980.[PMID: 39326669 PMCID: PMC11600309 DOI: 10.1016/j.jmoldx.2024.09.001]

29. Shurtleff MJ, Temoche-Diaz MM, Karfilis KV, et al. Y-box protein 1 is required to sort microRNAs into exosomes. *eLife.* 2016;5:e19276.[PMID: 27559612 PMCID: PMC5047747 DOI: 10.7554/eLife.19276]

30. Temoche-Diaz MM, Shurtleff MJ, Nottingham RM, et al. Distinct mechanisms of microRNA sorting into cancer cell-derived extracellular vesicle subtypes. *eLife.* 2019;8:e47544.[PMID: 31436530 PMCID: PMC6728143 DOI: 10.7554/eLife.47544]

31. Koppers-Lalic D, Hackenberg M, Bijnsdorp IV, et al. Nontemplated nucleotide additions distinguish the small RNA composition in cells from exosomes. *Cell Rep.* 2014;8:1649-58.[PMID: 25242326 DOI: 10.1016/j.celrep.2014.08.027]

32. Busatto S, Iannotta D, Walker SA, Di Marzio L, Wolfram J. A Simple and Quick Method for Loading Proteins in Extracellular Vesicles. *Pharmaceuticals (Basel).* 2021 Apr 13;14(4):356.[DOI: 10.3390/ph14040356. PMID: 33924377; PMCID: PMC8069621]

33. Waury K, Gogishvili D, Nieuwland R, Chatterjee M, Teunissen CE, Abeln S. Proteome encoded determinants of protein sorting into extracellular vesicles. *J Extracell Biol.* 2024 Jan 23;3(1):e120.[DOI: 10.1002/jex2.120. PMID: 38938677; PMCID: PMC11080751]

34. DaCunza JT, Wickman JR, Ajit SK. miRNA packaging into small extracellular vesicles and implications in pain. *Pain Rep.* 2024 Oct 23;9(6):e1198.[DOI: 10.1097/PR9.0000000000001198. PMID: 39450410; PMCID: PMC11500789]

35. Abdal Dayem A, Kwak Y, Jeun H, Cho SG. Recent Insights into Organoid-Derived Extracellular Vesicles and Their Biomedical Applications. *J Pers Med.* 2025 Oct 14;15(10):492.[DOI: 10.3390/jpm15100492. PMID: 41149854; PMCID: PMC12564934]

36. Pampaloni F, Reynaud EG, Stelzer EHK. The third dimension bridges the gap between cell culture and live tissue. *Nat Rev Mol Cell Biol.* 2007;8:839-45.[PMID: 17684528 DOI: 10.1038/nrm2236]

37. Edmondson R, Broglie JJ, Adcock AF, Yang L. Three-dimensional cell culture systems and their applications in drug discovery and cell-based biosensors. *Assay Drug Dev Technol.* 2014;12:207-18.[PMID: 24831787 PMCID: PMC4026212 DOI: 10.1089/adt.2014.573]

38. Baker BM, Chen CS. Deconstructing the third dimension: how 3D culture microenvironments alter cellular cues. *J Cell Sci.* 2012;125:3015-24.[PMID: 22797912 PMCID: PMC3434846 DOI: 10.1242/jcs.079509]

39. Breslin S, O'Driscoll L. Three-dimensional cell culture: the missing link in drug discovery. *Drug Discov Today.* 2013;18:240-9.[PMID: 23073387 DOI: 10.1016/j.drudis.2012.10.003]

40. Duval K, Grover H, Han LH, et al. Modeling physiological events in 2D vs. 3D cell culture. *Physiology.* 2017;32:266-77.[PMID: 28615311 PMCID: PMC5545611 DOI: 10.1152/physiol.00036.2016]

41. Fang Y, Eglen RM. Three-dimensional cell cultures in drug discovery and development. *SLAS Discov.* 2017;22:456472.[PMID: 28520521 PMCID: PMC5448717 DOI: 10.1177/1087057117696795]

42. Rocha S, Carvalho J, Oliveira P, et al. 3D cellular architecture affects microRNA and protein cargo of extracellular vesicles. *Adv Sci.* 2019;6:1800948.[PMID: 30828519 PMCID: PMC6382357 DOI: 10.1002/advs.201800948]

43. Thippabhotla S, Zhong C, He M. 3D cell culture stimulates the secretion of in vivo like extracellular vesicles. *Sci Rep.* 2019;9:13012.[PMID: 31506601 PMCID: PMC6736862 DOI: 10.1038/s41598-019-49671-3]

44. Carvalho J, Rocha S, Pereira R, et al. Proteomic and miRNA profiling of extracellular vesicles derived from 3D cancer cell cultures. *J Extracell Vesicles.* 2020;9:1796577.

45. Eckhardt CM, Baccarelli AA, Wu H. Environmental Exposures and Extracellular Vesicles: Indicators of Systemic Effects and Human Disease. *Curr Environ Health Rep.* 2022 Sep;9(3):465-76.[DOI: 10.1007/s40572-022-00357-5. Epub 2022 Apr 21. PMID: 35449498; PMCID: PMC9395256]

46. Javdani-Mallak A, Salahshoori I. Environmental pollutants and exosomes: A new paradigm in environmental health and disease. *Sci Total Environ.* 2024 May 15;925:171774.[DOI: 10.1016/j.scitotenv.2024.171774. Epub 2024 Mar 18. PMID: 38508246]

47. Dixson AC, Dawson TR, Di Vizio D, Weaver AM. Context-specific regulation of extracellular vesicle biogenesis and cargo selection. *Nat Rev Mol Cell Biol.* 2023 Jul;24(7):454-76.[DOI: 10.1038/s41580-023-00576-0. Epub 2023 Feb 10. PMID: 36765164; PMCID: PMC10330318]

48. Cook K, Ströhle G, Li H. Investigating the Impact of Various 2D and 3D Cell Culture Platforms on the Production of Extracellular Vesicles. *ACS Appl Bio Mater.* 2025 Sep 15;8(9):8218-29.[DOI: 10.1021/acsabm.5c01171. Epub 2025 Aug 28. PMID: 40873241]

49. Lane RE, Korbie D, Anderson W, et al. Analysis of exosome purification methods. *Sci Rep.* 2015;5:7639.[DOI: 10.1038/srep07639]

50. Clayton A, Buschmann D, Byrd JB, et al. Considerations towards a roadmap for collection, handling and storage of blood extracellular vesicles. *J Extracell Vesicles.* 2019;8:1647027.[PMID: 31489143 PMCID: PMC6711123 DOI: 10.1080/20013078.2019.1647027]

51. Welsh JA, Goberdhan DCI, O'Driscoll L, et al. Minimal information for studies of extracellular vesicles (MISEV2023): From basic to advanced approaches. *J Extracell Vesicles.* 2024 Feb;13(2):e12404.[DOI: 10.1002/jev2.12404] *Erratum in: J Extracell Vesicles.* 2024 May;13(5):e12451.[DOI: 10.1002/jev2.12451. PMID: 38326288; PMCID: PMC10850029]

52. Mitchell MI, Ben-Dov IZ, Liu C, et al. Extracellular Vesicle Capture by AnTibody of CHoice and Enzymatic Release (EV-CATCHER): A customizable purification assay designed for small-RNA biomarker identification and evaluation of circulating small-EVs. *J Extracell Vesicles.* 2021 Jun;10(8):e12110.[DOI: 10.1002/jev2.12110. Epub 2021 Jun 3. PMID: 34122779; PMCID: PMC8173589]

53. Mitchell MI, Ben-Dov IZ, Ye K, et al. Exhaled breath condensate contains extracellular vesicles (EVs) that carry miRNA cargos of lung tissue origin that can be selectively purified and analyzed. *J Extracell Vesicles.* 2024 Apr;13(4):e12440.[DOI: 10.1002/jev2.12440. *Erratum in: J Extracell Vesicles.* 2024 May;13(5):e12453.[DOI: 10.1002/jev2.12453. PMID: 38659349; PMCID: PMC11043690]

54. Loudig O, Ben-Dov IZ, Shapiro B, et al. Ultrasensitive cDNA Library Preparation for Next-generation Sequencing of MicroRNAs from Small Extracellular Vesicles. *J Vis Exp.* 2025 Jun 13;(220):10.3791/67154.[DOI: 10.3791/67154. PMID: 40587398; PMCID: PMC12269480]

55. Patil AH, Halushka MK. miRge3.0: a comprehensive microRNA and tRF sequencing analysis pipeline. *NAR Genom Bioinform.* 2021 Jul 21;3(3):lqab068.[DOI: 10.1093/nargab/lqab068. PMID: 34308351; PMCID: PMC8294687]

56. Wu C, Zhou S, Mitchell MI, Hou C, Byers S, Loudig O, Ma J. Coupling suspension trapping-based sample preparation and data-independent acquisition mass spectrometry for sensitive exosomal proteomic analysis. *Anal Bioanal Chem.* 2022 Mar;414(8):2585-95.[DOI: 10.1007/s00216-022-03920-z. Epub 2022 Feb 18. PMID: 35181835; PMCID: PMC9101639]

57. Mitchell MI, Ben-Dov IZ, Liu C, et al. Non-invasive detection of orthotopic human lung tumors by microRNA expression profiling of mouse exhaled breath condensates and exhaled extracellular vesicles. *Extracell Vesicles Circ Nucl Acids.* 2024;5(1):138-64.[DOI: 10.20517/evcna.2023.77. Epub 2024 Mar 28. PMID: 38863869; PMCID: PMC11165456]

58. Hou C, Li P, Pei E, Zhang H, et al. Site-Specific and Quantitative O-GlcNAc Proteomics for Hepatocellular Carcinoma. *J Proteome Res.* 2026 Apr 3;25(4):1892-902.[DOI: 10.1021/acs.jproteome.5c00939. Epub 2026 Mar 11. PMID: 41811088; PMCID: PMC13054871]

59. Farazi TA, Brown M, Morozov P, et al. Bioinformatic analysis of barcoded cDNA libraries for small RNA profiling by next-generation sequencing. *Methods.* 2012 Oct;58(2):171-87.[DOI: 10.1016/j.ymeth.2012.07.020. Epub 2012 Jul 23. PMID: 22836126; PMCID: PMC3597438]

60. Robinson MD, McCarthy DJ, Smyth GK. edgeR: a Bioconductor package for differential expression analysis of digital gene expression data. *Bioinformatics.* 2010 Jan 1;26(1):139-40.[DOI: 10.1093/bioinformatics/btp616. Epub 2009 Nov 11. PMID: 19910308; PMCID: PMC2796818]

61. Love MI, Huber W, Anders S. Moderated estimation of fold change and dispersion for RNA-seq data with DESeq2. *Genome Biol.* 2014;15(12):550.[DOI: 10.1186/s13059-014-0550-8. PMID: 25516281; PMCID: PMC4302049]

62. Gaujoux R, Seoighe C. A flexible R package for nonnegative matrix factorization. *BMC Bioinformatics.* 2010 Jul 2;11:367.[DOI: 10.1186/1471-2105-11-367. PMID: 20598126; PMCID: PMC2912887]

63. Dennis G Jr, Sherman BT, Hosack DA, et al. DAVID: Database for Annotation, Visualization, and Integrated Discovery. *Genome Biol.* 2003;4(5):P3. Epub 2003 Apr 3.[PMID: 12734009]

64. Supek F, Bošnjak M, Škunca N, Šmuc T. REVIGO summarizes and visualizes long lists of gene ontology terms. *PLoS One.* 2011;6(7):e21800.[DOI: 10.1371/journal.pone.0021800. Epub 2011 Jul 18. PMID: 21789182; PMCID: PMC3138752]

65. Dweep H, Gretz N, Sticht C. miRWalk database for miRNA-target interactions. *Methods Mol Biol.* 2014;1182:289-305.[DOI: 10.1007/978-1-4939-1062-5_25. PMID: 25055920]

66. Sticht C, De La Torre C, Parveen A, Gretz N. miRWalk: An online resource for prediction of microRNA binding sites. *PLoS One.* 2018 Oct 18;13(10):e0206239.[DOI: 10.1371/journal.pone.0206239. PMID: 30335862; PMCID: PMC6193719]

67.Thippabhotla S, Zhong C, He M. 3D cell culture stimulates the secretion of in vivo like extracellular vesicles. *Sci Rep.* 2019 Sep 10;9(1):13012.[DOI: 10.1038/s41598-019-49671-3. PMID: 31506601; PMCID: PMC6736862]

68. Weng Q, Wang Y, Xie Y, et al. Extracellular vesicles-associated tRNA-derived fragments (tRFs): biogenesis, biological functions, and their role as potential biomarkers in human diseases. *J Mol Med (Berl).* 2022 May;100(5):679-95.[DOI: 10.1007/s00109-022-02189-0. Epub 2022 Mar 24. PMID: 35322869; PMCID: PMC9110440]

69. Colombo M, Raposo G, Théry C. Biogenesis, secretion, and intercellular interactions of exosomes and other extracellular vesicles. *Annu Rev Cell Dev Biol.* 2014;30:255-89.[DOI: 10.1146/annurev-cellbio-101512-122326. Epub 2014 Aug 21. PMID: 25288114]

70. van Niel G, D'Angelo G, Raposo G. Shedding light on the cell biology of extracellular vesicles. *Nat Rev Mol Cell Biol.* 2018 Apr;19(4):213-28.[DOI: 10.1038/nrm.2017.125. Epub 2018 Jan 17. PMID: 29339798]

71. Théry C, Witwer KW, Aikawa E, et al. Minimal information for studies of extracellular vesicles 2018 (MISEV2018): a position statement of the International Society for Extracellular Vesicles and update of the MISEV2014 guidelines. *J Extracell Vesicles.* 2018 Nov 23;7(1):1535750.[DOI: 10.1080/20013078.2018.1535750. PMID: 30637094; PMCID: PMC6322352]

72. Thippabhotla S, Zhong C, He M. 3D cell culture stimulates the secretion of in vivo like extracellular vesicles. *Sci Rep.* 2019 Sep 10;9(1):13012.[DOI: 10.1038/s41598-019-49671-3. PMID: 31506601; PMCID: PMC6736862]

73. Ai Y, Guo C, Garcia-Contreras M, et al. Endocytosis blocks the vesicular secretion of exosome marker proteins. *Sci Adv.* 2024 May 10;10(19):eadi9156.[DOI: 10.1126/sciadv.adi9156. Epub 2024 May 8. PMID: 38718108; PMCID: PMC11078179]

74. Andreu Z, Yáñez-Mó M. Tetraspanins in extracellular vesicle formation and function. *Front Immunol.* 2014 Sep 16;5:442.[DOI: 10.3389/fimmu.2014.00442. PMID: 25278937; PMCID: PMC4165315]

75. Kowal J, Arras G, Colombo M, et al. Proteomic comparison defines novel markers to characterize heterogeneous populations of extracellular vesicle subtypes. *Proc Natl Acad Sci U S A.* 2016 Feb 23;113(8):E968-77.[DOI: 10.1073/pnas.1521230113. Epub 2016 Feb 8. PMID: 26858453; PMCID: PMC4776515]

76. Mathieu M, Martin-Jaular L, Lavieu G, Théry C. Specificities of secretion and uptake of exosomes and other extracellular vesicles for cell-to-cell communication. *Nat Cell Biol.* 2019 Jan;21(1):9-17.[DOI: 10.1038/s41556-018-0250-9. Epub 2019 Jan 2. PMID: 30602770]

77. Loudig O, Liu C, Rohan T, Ben-Dov IZ. Retrospective MicroRNA Sequencing: Complementary DNA Library Preparation Protocol Using Formalin-fixed Paraffin-embedded RNA Specimens. *J Vis Exp.* 2018 May 5;(135):57471.[DOI: 10.3791/57471. PMID: 29781987; PMCID: PMC6101110]

78. Valadi H, Ekström K, Bossios A, Sjöstrand M, Lee JJ, Lötvall JO. Exosome-mediated transfer of mRNAs and microRNAs is a novel mechanism of genetic exchange between cells. *Nat Cell Biol.* 2007 Jun;9(6):654-9.[DOI: 10.1038/ncb1596. Epub 2007 May 7. PMID: 17486113]

79. Vickers KC, Palmisano BT, Shoucri BM, Shamburek RD, Remaley AT. MicroRNAs are transported in plasma and delivered to recipient cells by high-density lipoproteins. *Nat Cell Biol.* 2011 Apr;13(4):423-33.[DOI: 10.1038/ncb2210. Epub 2011 Mar 20. *Erratum in: Nat Cell Biol.* 2015 Jan;17(1):104. PMID: 21423178; PMCID: PMC3074610]

80. Yáñez-Mó M, Siljander PR, Andreu Z, et al. Biological properties of extracellular vesicles and their physiological functions. *J Extracell Vesicles.* 2015 May 14;4:27066.[DOI: 10.3402/jev.v4.27066. PMID: 25979354; PMCID: PMC4433489]

81. Villarroya-Beltri C, Gutiérrez-Vázquez C, Sánchez-Cabo F, et al. Sumoylated hnRNPA2B1 controls the sorting of miRNAs into exosomes through binding to specific

motifs. *Nat Commun.* 2013;4:2980.[DOI: 10.1038/ncomms3980. PMID: 24356509; PMCID: PMC3905700]

82. Santangelo A, Imbrucè P, Gardenghi B, et al. A microRNA signature from serum exosomes of patients with glioma as complementary diagnostic biomarker. *J Neurooncol.* 2018 Jan;136(1):51-62.[DOI: 10.1007/s11060-017-2639-x. Epub 2017 Oct 26. PMID: 29076001]

83. Shurtleff MJ, Yao J, Qin Y, Nottingham RM, Temoche-Diaz MM, Schekman R, Lambowitz AM. Broad role for YBX1 in defining the small noncoding RNA composition of exosomes. *Proc Natl Acad Sci U S A.* 2017 Oct 24;114(43):E8987-95.[DOI: 10.1073/pnas.1712108114. Epub 2017 Oct 10. PMID: 29073095; PMCID: PMC5663387]

84. Tosar JP, Segovia M, Castellano M, et al. Fragmentation of extracellular ribosomes and tRNAs shapes the extracellular RNAome. *Nucleic Acids Res.* 2020 Dec 16;48(22):12874-88.[DOI: 10.1093/nar/gkaa674. PMID: 32785615; PMCID: PMC7736827]

85. Lv D, Hu Z, Lu L, Lu H, Xu X. Three-dimensional cell culture: A powerful tool in tumor research and drug discovery. *Oncol Lett.* 2017 Dec;14(6):6999-7010.[DOI: 10.3892/ol.2017.7134. Epub 2017 Oct 3. PMID: 29344128; PMCID: PMC5754907]

86. Zhou Y, Yu F, Guo M, Tang Y, Xu Q. Bridging the gap: the role of 3D cell cultures in mimicking tumor microenvironment for enhanced drug testing accuracy. *Front Bioeng Biotechnol.* 2025 Aug 12;13:1498141.[DOI: 10.3389/fbioe.2025.1498141. PMID: 40873434; PMCID: PMC12378905]

87. Fontana F, Marzagalli M, Sommariva M, Gagliano N, Limonta P. In Vitro 3D Cultures to Model the Tumor Microenvironment. *Cancers (Basel).* 2021 Jun 13;13(12):2970.[DOI: 10.3390/cancers13122970. PMID: 34199324; PMCID: PMC8231786]